Cortical glutamatergic projection neuron types contribute to distinct functional subnetworks

Hemanth Mohan[1,2], Xu An[1,2], Hideki Kondo[2], Shengli Zhao[1], Simon Musall[2,3], Partha Mitra[1], Z. Josh Huang[1,2,*]

[1]Department of Neurobiology, Duke University Medical Center, Durham, NC 27710, USA

[2]Cold Spring Harbor Laboratory, Cold Spring Harbor, NY 11724, USA.

[3] Institute of Biological information Processing,Forschungszentrum Julich, Julich, Germany

[*]corresponding author: josh.huang@duke.edu

Abstract

The cellular basis of cerebral cortex functional architecture remains not well understood. A major challenge is to monitor and decipher neural network dynamics across broad cortical areas yet with projection neuron (PN) type resolution in real time during behavior. Combining genetic targeting and wide-field imaging, we monitored activity dynamics of subcortical-projecting (PT^{Fezf2}) and intratelencephalic-projecting (IT^{PlxnD1}) types across dorsal cortex of mice during multiple brain states and behaviors. IT^{PlxnD1} and PT^{Fezf2} showed distinct activation patterns during wakeful resting, spontaneous movements, and upon sensory stimulation. Distinct IT^{PlxnD1} and PT^{Fezf2} subnetworks dynamically tuned to different sensorimotor components of a naturalistic feeding behavior, and optogenetic inhibition of subnetwork nodes disrupted specific behavioral components. IT^{PlxnD1} and PT^{Fezf2} projection patterns supported their subnetwork activation patterns. Our results suggest that, in addition to the concept of columnar organization, dynamic areal and PN type-specific subnetworks is a key feature of cortical functional architecture linking microcircuit components with global brain networks.

Introduction

The cerebral cortex orchestrates high-level brain functions ranging from perception and cognition to motor control, but the cellular basis of cortical network organization remains not well understood. Across mammalian species, the cortex consists of dozens to over a hundred cortical areas, each featuring specific input-output connections with multiple other areas, thereby forming numerous functional subnetworks of information processing (Bota et al., 2015; Van Essen and Glasser, 2018). Within each area, seminal discoveries have revealed columnar organization of neurons with similar functional properties (Hubel and Wiesel, 1963; Mountcastle et al., 1957), a foundational concept that has guided decades of cortical research (Hubel David and Wiesel Torsten, 2005). Across multiple cortical layers, diverse neuron types form intricate connectivity, thought to be based upon a "canonical circuit" template that is duplicated and modified across areas (Douglas and Martin, 2007; Harris and Shepherd, 2015; Markram et al., 2015). An enduring challenge is to decipher the cellular basis of cortical architecture characterized by such nested levels of organization that integrates cellular microcircuits with global areal and brain networks across spatiotemporal scales (Engel et al., 2021; Lerner et al., 2016).

Among diverse cortical cell types, glutamatergic pyramidal neurons (PNs) constitute key elements for constructing the cortical architecture (Harris and Shepherd, 2015; Huang, 2014): whereas their cross-laminar dendrites and local axonal arbors form the skeleton of cortical microcircuits, their long-range axons mediate all the intracortical processing streams and subcortical output channels. PNs consist of diverse projection types hierarchically organized into several top-levels classes, each comprising finer grained projection types (Harris and Shepherd, 2015; Tasic et al., 2018). Whereas the pyramidal track PNs (PT class) mediate all cortical output channels, intratelencephalic PNs (IT class) underlie myriad intracortical processing streams. Recent studies in rodents have achieved a comprehensive anatomic description of cortical areal subnetworks (Gamanut et al., 2018; Zingg et al., 2014) and begin to reveal their cellular underpinnings (Harris et al., 2019; Munoz-Castaneda et al., 2021). However, the cellular basis of functional cortical networks remains poorly understood, as such studies require methods to monitor neural activity patterns across large swaths of cortical territory yet with cell type resolution in real time and in behaving animals.

Traditional fMRI studies measure brain metabolic activities as a proxy of neural activity but with poor spatiotemporal resolution and no cellular resolution (Gozzi and Schwarz, 2016; Smith et al., 2013). Conversely, single unit recording (Steinmetz et al., 2021) and two-photon calcium imaging (Svoboda et al., 1999) achieve cellular and real-time temporal resolution but with limited spatial coverage. Recent advances in widefield calcium imaging in rodent cortex provide an opportunity to bridge cellular and cortex-wide measurement of neural activity (Cardin et al., 2020). However, most studies to date have imaged cortex wide activity of broad neuronal classes (Allen et al., 2017; Musall et al., 2019; Wekselblatt et al., 2016) or laminar subpopulations containing mixed projection types (Gilad et al., 2018; Kauvar et al., 2020; Ma et al., 2016; Vesuna et al., 2020; Xiao et al., 2017), thus have yet to resolve and compare distinct PN projection types in cortical network operations. In particular, whether

and how IT and PT PNs, two major top-level projection classes, differentially and coordinately contribute to cortical processing networks remain unclear.

We have recently generated a comprehensive genetic toolkit for targeting the hierarchical organization of PNs in mouse cerebral cortex (Matho et al., 2021). Here, we performed wide-field calcium imaging of the activation dynamics of genetic and projection defined IT^{PlxnD1} and PT^{Fezf2} subpopulations across the dorsal cortex of head-fixed mice during multiple brain states and sensory-motor behaviors, an approach that enabled a cell type resolution integration of anatomical and functional analysis of cortical subnetworks. We found that IT^{PlxnD1} and PT^{Fezf2} show distinct activity dynamics during wakeful resting, spontaneous movements, upon sensory stimulation, as well as during dissociation-like state under anesthesia. Furthermore, we revealed distinct IT^{PlxnD1} and PT^{Fezf2} subnetworks dynamically tuned to different sensorimotor components of a naturalistic feeding behavior, which involves food retrieval and coordinated mouth-hand movements during eating; optogenetic inhibition of key cortical nodes in these subnetworks disrupted specific components of this behavior. Anterograde tracing of IT^{PlxnD1} and PT^{Fezf2} from key cortical nodes revealed projection patterns that contribute to functional activation patterns of corresponding subnetworks. Together, these results demonstrate that IT and PT subpopulations operate across distinct and parallel cortical processing streams and output pathways with divergent spatiotemporal dynamics; they suggest that, in addition to the concept of columnar organization, dynamic areal and PN type-specific subnetworks is a key feature of cortical functional architecture that integrates across nested levels from microcircuit components to global brain networks.

Results

Although wide-field mesoscopic calcium imaging in rodents has the potential to reveal the cellular basis of functional cortical networks, the full realization of this potential critically depends on the resolution for distinguishing different PN types through specific expression of genetic encoded calcium sensors. To date, most if not all these studies examined subpopulation (e.g. those defined by Thy1 and Rbp4 transgenic lines) comprising mixtures of different projection classes (Kauvar et al., 2020; Ma et al., 2016; Vesuna et al., 2020; Xiao et al., 2017), which precluded a direct and clear link between projection and function defined cortical networks. We have recently generated gene knockin mouse driver lines that enable specific genetic access to hierarchical PN classes and subpopulations within the class (Matho et al., 2021). Among these, the *Fezf2-CreER* line captures the large majority of PT population (PT^{Fezf2}) in layer 5b and 6, and the *PlxnD1-CreER* captures an IT subpopulation (IT^{PlxnD1}) which resides in both L2/3 and L5a (Matho 2021). Whereas PTs^{Fezf2} project to contralateral subcortical targets and represent over 95% of corticospinal projection neurons (Matho 2021), ITs^{PlxnD1} project to ipsi- and contra-lateral cortical and striatal targets. As IT is the largest and most diverse PyN class comprising intracortical, callosal, and cortico-striatal PyNs across layer 2-6, using double mRNA in situ hybridization we estimated that *PlxnD1* represent about 63% of IT neurons marked by *Satb2* (Fig. 1b). Quantification of cell distribution using serial two-photon tomography (STP) and CCF (mouse brain Common Coordinate Framework) registration demonstrated that PT^{Fezf2} and IT^{PlxnD1} are

distributed across the entire dorsal neocortex (Fig, 1a, Matho 2021). Therefore, *Fezf2*- and *PlxnD1*-driver lines represent specific and reliable tools that categorically distinguish the top-level PT and IT classes.

Distinct cortical activation patterns of IT^{PlxnD1} and PT^{Fezf2} during quiescent resting state and spontaneous movements

To examine IT^{PlxnD1} and PT^{Fezf2} activation patterns reflected by their calcium dynamics, we bred *PlxnD1* and *Fezf2* driver lines with a Cre-activated GCaMP6f reporter line (Ai148). Using serial two-photon tomography (STP), we found global GCaMP6f expression for each cell type across all regions of the dorsal cortex (consistent with Matho 2021).As expected, GCaMP6f expression was restricted to L2/3 and 5a PyNs in *PlxnD1* mice, and to L5b and to a lower extent in L6 PyNs in *Fezf2* mice (Fig. 1a.). We first characterized network dynamics of IT^{PlxnD1} and PT^{Fezf2} during wakeful resting state in head-fixed mice using epifluorescence wide-field imaging to measure neuronal activity across the dorsal cortex. During this state, animals alternated between quiescence and spontaneous whisker, forelimb, and orofacial movements (Suppl. Videos 1,2). We quantified full frame variance from behavioral videos recorded simultaneously with wide-field GCaMP6f imaging and identified episodes of quiescence and movements (active, Fig. 1c, methods). We measured standard deviations of neural activity for all pixels in each episode and found significantly higher activity during spontaneous movements versus quiescent episode in both cell types (Suppl. Fig. 1b). We then measured the peak normalized variance per pixel to obtain a cortical activation map during each episode. While both IT^{PlxnD1} and PT^{Fezf2} were active across broad areas, they differed significantly in strongly active areas (Fig 1d, Suppl Fig. 1a). In quiescent episodes, IT^{PlxnD1} were most active across forelimb, hindlimb, and frontolateral regions while PT^{Fezf2} were strongly active in posteromedial parietal areas. During spontaneous movement episodes, IT^{PlxnD1} showed strong activation in hindlimb and visual sensory areas while PT^{Fezf2} showed localized activation in the posteromedial parietal regions, with lower activation in other regions (Fig. 1d, Suppl Fig. 1a).

To investigate the correlation between neural activity and spontaneous movements, we built a linear encoding model using the top 200 singular value decomposition (SVD) temporal components of the behavior video as independent variables to explain the top 200 SVD temporal components of activity dynamics. By measuring the proportion of 5-fold cross-validated activity variance explained by spontaneous movements (Methods), we found PT^{Fezf2} neural activity to be more strongly associated with spontaneous movements compared to IT^{PlxnD1} (Fig 1e, Methods). We then extracted mean time varying variance from parts of the behavior video frames covering nose, mouth, whisker, and forelimb regions (Fig. 1f inset) and identified the proportion of neural variance accounted by each body movement. While whisker and mouth contributed to some extent and equally between the two PyN types, forelimbs contributed significantly larger fraction of neural activity to PT^{Fezf2} than IT^{PlxnD1} (Fig. 1f, methods). We transformed the forelimb regression weights to the spatial domain of the neural activity (methods) and find parietal region to be most active in PT^{Fezf2} while IT^{PlxnD1} was active within forelimb-hindlimb sensory areas (Suppl. Fig 1e). To measure the reliability of the resting state activity patterns we quantified Pearson's correlation between spatial maps across mice and session and found strong correlation within and weak correlation between PN types (Suppl. Fig 1c) during quiescent

episode. During spontaneous movement episodes, IT^{PlxnD1} activity maps were far more variable compared to PT^{Fezf2} (Suppl Fig 1d). Principal component analysis on the combined spatial maps of both PyN types revealed non-overlapping clusters across both episodes, indicating distinct cortical activation patterns between IT^{PlxnD1} and PT^{Fezf2} (Suppl. Fig. 1f,g). Together, these results demonstrate distinct activation patterns of IT^{PlxnD1} and PT^{Fezf2} during wakeful resting state, and preferential PT^{Fezf2} activation in parietal cortex associated with spontaneous movements compared to IT^{PlxnD1}.

Unimodal sensory inputs preferentially activate IT^{PlxnD1} but not PT^{Fezf2}

We next investigated cortical activation of IT^{PlxnD1} and PT^{Fezf2} following sensory inputs of the somatosensory and visual system (Fig. 1g, methods). We computed mean response across time for the stimulus duration associated with whisker, orofacial and visual stimulation to identify activated cortical areas (Fig. 1h.). Light stimulation and tactile stimulation of whisker and orofacial region strongly activated IT^{PlxnD1} in primary visual, whisker and mouth-nose somatosensory cortex but resulted in no or weak activation of PT^{Fezf2} in those cortical areas (Fig 1h). To compare response intensities, we identified centers of maximum activation from the IT^{PlxnD1} spatial maps and extracted temporal signals within a circular window around the centers and computed single trial dynamics and trial averaged responses from both PyN types (Fig. 1i-k). Again, we found strong IT^{PlxnD1} activation and very weak or no PT^{Fezf2} activation in primary sensory cortices in response to whisker, orofacial, and visual stimulus (Fig. 1j,k). We measured response intensities by integrating the signal for the stimulus duration and found significantly higher activity in IT^{PlxnD1} compared to PT^{Fezf2} (Fig. 1k). To visualize cortical regions active irrespective of response intensity, we peak normalized the maps and found activation in corresponding sensory cortices in PT^{Fezf2} along with broader activation including the retrosplenial areas (Suppl. Fig. 2a). We measured the reliability of activation patterns by computing the Pearson's correlation between the spatial maps across mice and sessions and find strong correlation between IT^{PlxnD1} spatial maps compared to PT^{Fezf2} (Suppl. Fig. 2b). These results provide the first set of in vivo evidence that sensory inputs predominantly activate IT compared to PT PNs and that IT activation per se does not lead to significant PT activation. These results are consistent with previous findings that thalamic input predominantly impinges on IT but not PT cells (Shepherd and Yamawaki, 2021). Surprisingly, IT activation per se does not lead to significant PT activation, despite demonstrated synaptic connectivity from in vitro studies (Hooks, 2017).

Distinct PT^{Fezf2} and IT^{PlxnD1} subnetworks tuned to different sensorimotor components of a feeding behavior

To examine the activation patterns of IT^{PlxnD1} and PT^{Fezf2} during sensorimotor processing, we designed a head-fixed setup that captures several features of naturalistic mouse feeding behavior. In this setup, mice sense a food pellet approaching from the right side on a moving belt, retrieve pellet into mouth by licking, recruit both hands to hold pellet, then initiate repeated bouts of hand-mouth coordinated eating movements that include: bite while handling the pellet, transfer pellet to hands while chewing, raise hands to bring pellet to mouth thereby starting the next bout (Fig. 2a, Suppl video 3). We used DeepLabCut (Mathis et al., 2018) to track pellet and body parts in video recordings and wrote custom algorithms to identify and annotate major events in successive phases of this behavior (methods, Fig. 2b).

We then imaged the spatiotemporal activation patterns of IT^{PlxnD1} and PT^{Fezf2} across dorsal cortex while mice engage in the behavior (Suppl. Videos 4,5). We calculated average GCaMP6f signals per pixel in frames taken at multiple time points centered around when mice retrieve pellet into the mouth (pellet-in-mouth, or PIM) (Fig. 2c, frames displayed at 200ms time steps). Upon sensing pellet approaching from the right side, mice adjust their postures and limb grips of the supporting hand bar while initiating multiple right-directed licks until retrieving the pellet into the mouth. During this period (Fig.2c, -0.7-0 seconds), IT^{PlxnD1} was first activated in left whisker primary sensory cortex (SS_{bfd}), which then spread to bi-lateral forelimb and hindlimb sensory areas (Fig 2c, Suppl. Video 4). Almost simultaneously or immediately after, PT^{Fezf2} was strongly activated in left medial parietal cortex (parietal node) just prior to right-directed licks, followed by bi-lateral activation in frontal cortex (medial secondary motor cortex, frontal node) during lick and pellet retrieval into mouth (Fig 2c, Suppl. Video 5). During the brief PIM period when mice again adjusted postures and then lift both hands to hold the pellet (Fig 2c, 0-0.1 sec), IT^{PlxnD1} was activated in bi-lateral orofacial primary sensory cortex (frontolateral posterior node (FLP)) and subsequently in an anterior region spanning the lateral primary and secondary motor cortex (frontolateral anterior node (FLA)), while PT^{Fezf2} activation shifted from bi-lateral frontal to parietal node. In particular, PT^{Fezf2} activation in parietal cortex reliably preceded hand lift. Following the initiation of repeated bouts of eating actions, IT^{PlxnD1} was prominently activated in bilateral FLA and FLP specifically during coordinated oral-manual movements such as biting and handling, whereas PT^{Fezf2} activation remained minimum throughout the dorsal cortex. Notably, both IT^{PlxnD1} and PT^{Fezf2} showed much reduced activation during chewing.

To obtain a spatial map of cortical activation during specific feeding events, we build a linear encoding model using binary time stamps associated with the duration of lick, pellet-in-mouth, hand lift, handling, and chewing as independent variables to explain the top 200 SVD temporal components of neural activity. We then transformed the regression weights obtained from the model to the spatial domain of neural activity using the SVD spatial components to obtain a cortical map of weights associated with each event (methods, Fig. 2d). This analysis largely confirmed and substantiated our initial observations [manual annotations] (Fig. 2c). Indeed, during lick onset IT^{PlxnD1} was active in left barrel cortex and bilateral forelimb/hindlimb sensory areas, which correlated with sensing the approaching pellet with contralateral whiskers and limb adjustments, respectively. In sharp contrast, PT^{Fezf2} was active along a medial parietal-frontal axis, which correlated with licking. During PIM, IT^{PlxnD1} was preferentially active in FLP with lower activity in FLA as well as in forelimb/hindlimb sensory areas, while PT^{Fezf2} was still active along the parietofrontal regions. Prior to and during hand lift, PT^{Fezf2} showed strongly activation specifically in bilateral parietal areas, whereas IT^{PlxnD1} showed predominant bilateral activation in both FLA and FLP. During eating and pellet handling, IT^{PlxnD1} was strongly active in FLA and less active in FLP, while PT^{Fezf2} was only weakly active specifically in the frontal node (Fig 2d, notice the change in scale). Both IT^{PlxnD1} and PT^{Fezf2} showed significantly reduced activity across the dorsal cortex during chewing (Fig. 2d).
To capture the most prominently activated cortical areas associated with key events of the behavior, we computed average activity per pixel during the progression from licking, retrieving pellet into mouth, to hand lift across mice and sessions (from 1 second before to 2 seconds after pellet-in-mouth). This

analysis confirmed that, while both cell populations were activated across multiple regions, PT^{Fezf2} activation was most prominent across a medial parietal-frontal network whereas IT^{PlxnD1} was most strongly engaged across a frontolateral FLA-FLP network (Fig. 3a,d). To characterize the temporal activation patterns of these key cortical nodes during behavior, we extracted temporal traces from the center within each of these 4 areas (averaged across pixels within a 280 µm radius circular window) and examined their temporal dynamics aligned to the onset of lick, pellet-in-mouth, and hand lift (Fig 3 b,c,e,f). PT^{Fezf2} activities in the frontal node rose sharply prior to lick, sustained for the duration of lick until PIM, then declined prior to hand lift; on the other hand, PT^{Fezf2} activities in the parietal node increased prior to lick then declined immediately after, followed by another sharp increase prior to hand lift then declined again right after. In contrast, IT^{PlxnD1} activities in FLA and FLP did not modulate significantly during either licking or hand lift but increased specifically only when mice first retrieved pellet into mouth; while activation in FLP decreased following a sharp rise after pellet-in-mouth, activities in FLA sustained during biting and handling (Fig. 3 g,i).

To examine the more precise temporal relationship between the activation of these nodes, we measured the peak rate of change of signals centered to PIM for IT^{PlxnD1} and lick onset for PT^{Fezf2}. IT^{PlxnD1} activities in FLP showed a steeper increase compared to FLA while PT^{Fezf2} activities in parietal node rose more sharply compared to the frontal node. These results suggest that FLP was activated prior to FLA within IT^{PlxnD1} and parietal was activated prior to frontal within PT^{Fezf2} (Fig. 3h,j). To examine cortical dynamics from both populations within the same region, we measured GCaMP6f signals centered to PIM from all four nodes for each cell type. PT^{Fezf2} showed strong activation within parietal and frontal nodes specifically during lick and hand lift, whereas IT^{PlxnD1} showed significantly lower activation within these nodes during these episodes (Fig. 3k,l). In sharp contrast, IT^{PlxnD1} was preferentially active in FLA and FLP specifically during PIM with sustained activity especially in FLA during biting and handling, but no associated activity was observed in PT^{Fezf2} within these nodes during the same period (Fig. 3k,l).

To validate the differential temporal dynamics between PN types we performed linear discriminant analysis (LDA) on combined single trails of IT^{PlxnD1} and PT^{Fezf2} in each node (methods). We projected single traces onto the top two dimensions identified by LDA to visualize the spatial distribution of projected clusters. This analysis revealed that IT^{PlxnD1} and PT^{Fezf2} clustered independently with little overlap, indicating that these PNs follow distinct temporal dynamics within each region (Fig. 3m). Altogether, these results indicate that IT^{PlxnD1} and PT^{Fezf2} operate in distinct and partially parallel cortical subnetworks, which are differentially engaged during specific sensorimotor components of an ethologically relevant behavior.

Feeding without hand occludes parietal PT^{Fezf2} activity

To investigate if the observed PN neural dynamics were causally related to features of the feeding behavior, we developed a variant of the feeding task in which mice lick to retrieve food pellet but eat without using hands (Fig. 4a); this was achieved by using a blocking plate to prevent hand lift until mice no longer attempted to use hand during eating. We then measured IT^{PlxnD1}activity in FLA-FLP nodes and PT^{Fezf2} activities in parietal-frontal nodes aligned to the onset of lick and PIM, and compared

activity dynamics to those during normal trials in the same mice when they used hands to eat (Fig. 4b-e). Whereas PT^{Fezf2} activities in the frontal node did not show a difference with or without hand lift (Fig 4c), PT^{Fezf2} activities in parietal showed a significant decrease in trials without hand lift specifically during the time when mice would have lifted hand during normal feeding trials. On the other hand, IT^{PlxnD1} activities in FLA and FLP did not change for the duration from retrieving pellet through hand lift in trials with no hand lift compared with those in normal trials with hand lift. However, IT^{PlxnD1} activities in FLA and FLP showed a notable reduction during the eating-handling phase (Fig. 4d,e). We then computed activity integral from PIM onset to 1 second after and compared results between trials with and without hand lift. Only PT^{Fezf2} activities in parietal node showed a sharp decline whereas IT^{PlxnD1} activities across FLA and FLP did not change significantly during the hand lift phase.

To visualize cortical regions differentially modulated between feeding trials with or without hand-lift, we computed mean pixel-wise activity during a 1 second period after PIM onset from both trial types and subtracted the spatial map of no-hand-lift trials from that of hand-lift trials. As expected parietal activity was much higher in PT^{Fezf2} during hand-lift compared to no-hand-lift trials (Fig. 4h,i). These results provide a causal linking between parietal PT^{Fezf2} activation and hand lift movement during feeding; they also indicate that IT^{PlxnD1} activity in FLA and FLP is in part related to sensorimotor components of mouth feeding actions.

Inhibition of parietofrontal and frontolateral subnetworks differentially disrupts sensorimotor components of feeding behavior

To investigate the causal contribution of parietofrontal and frontolateral networks in pellet feeding behavior, we adopted a laser scanning method to optogenetically inhibit bilateral regions of dorsal cortex using vGat-ChR2 mice expressing Channelrhodopsin-2 in GABAergic interneurons. We examined the effects of bilateral inhibition of parietal, frontal, FLP and FLA nodes on different components of the behavior including pellet retrieval by licking, hand lift after PIM, and mouth-hand mediated eating bouts. We pooled the data from FLA and FLP as we did not observe major differences in disrupting each of the two areas.

During the pellet retrieval phase, inhibition of frontal and the frontolateral nodes prior to lick onset resulted in a sharp decrease of tongue extension, which recovered after about 0.5 seconds (Fig. 5b,c); inhibition also led to a significant delay and disruption in pellet retrieval to mouth (Fig. 5d). These effects were not observed by inhibiting the parietal node (Fig. 5b-d). During the hand-lift phase after PIM, inhibition of frontal and frontolateral nodes prior to hand lift onset led to substantial deficit in the ability to lift hands towards mouth, resulting in a sharp decrease in the number of hand lift (Fig. 5e); notably, in trials when animals did initiate hand lift despite inhibition, hand trajectories appeared smooth and normal. Upon inhibiting the parietal node, on the other hand, no significant decrease of hand lift per se was observed but there were substantial deficits in hand lift trajectory, characterized by erratic and jerky movements (Fig. 5e). To quantify these deficits, we measured the absolute value of the first derivative to obtain the time varying velocity during the lift episode and compared its integral between 0 to 1 second after hand lift between inhibition and control trials. While frontal and frontolateral inhibition did not affect lift trajectories among the successful trials, parietal inhibition

resulted in a significant modulation of velocity during lift, indicating deficits in coordinating hand movements (Fig. 5f,g).

During eating bouts with coordinated mouth-hand movements after the initial hand lift from the hand bar to hold pellet in mouth, inhibiting the frontal and frontolateral nodes severely impeded mice's ability to bring pellet to mouth (i.e. secondary hand lifts when mice bring pellet to mouth after holding it while chewing) ; this deficit recovered immediately after the release of inhibition. Inhibiting the parietal node resulted in only a slight disruption of these secondary hand lifts (Fig. 5h). To quantify these deficits, we measured the average distance of left fingers to the mouth, number of secondary hand lifts, and the duration of the hand held close to mouth. We found significant deficits in all these parameters in inhibition trials for all four cortical areas compared to those of control trials (Fig. 5i-k). Furthermore, during eating mice normally handle the pellet while biting with repeated grasp-release movements (Fig. 5l). Inhibiting the frontal and frontolateral nodes substantially decreased the number of handling movements, with a more prominent effect during frontolateral inhibition (Fig. 5m). These results suggest that the parietofrontal and frontolateral networks differentially contribute to orchestrating orofacial and forelimb movements that enable pellet retrieval and mouth-hand coordinated eating behavior. Considering the spatiotemporal activation patterns of PT^{Fezf2} and IT^{PlxnD1} during this behavior (Fig. 2, 3), it is likely that PT^{Fezf2} might mainly contribute to the function of parietofrontal network and IT^{PlxnD1} might mainly contribute to the function of frontolateral network.

Distinct projection patterns of IT^{PlxnD1} frontolateral and PT^{Fezf2} parietofrontal subnetworks

To explore the anatomical basis and IT^{PlxnD1} and PT^{Fezf2} subnetworks revealed by wide-field calcium imaging, we examined their projection patterns by anterograde tracing using recombinase-dependent AAV in driver mouse lines. Using serial two photon tomography (STP) across the whole mouse brain (ref, Osten), we extracted the brain wide axonal projections and registered them to the Allen mouse Common Coordinate Framework (CCFv3, methods, (Niedworok et al., 2016; Tyson et al., 2021)). Using 3D masks generated from the CCF-registered map for each brain, we quantified and projected axonal traces within specific regions across multiple planes. Using an isocortex mask, we extracted axonal traces specifically within the neocortex and projected signals to the dorsal cortical surface (Fig. 6a).

As expected, PT^{Fezf2} in parietal and frontal region show very little intracortical projections (Fig 6a, Suppl, Fig. 3a), thus we focused on characterizing their subcortical targets (Fig. 6b-f). PT^{Fezf2} in frontal node predominantly project to dorsal striatum, pallidum (PAL), sensorimotor and polymodal thalamus (THsm, THpm), hypothalamus (HY), motor and behavior state related midbrain regions (MBmot, MBsat), and motor and behavior state related Pons within the hindbrain (P-mot, P-sat, Fig 6b). PT^{Fezf2} in parietal node projected to a similar set of subcortical regions as those of frontal node, but often at topographically different locations within each target region (Fig. 6b-f). To analyze the projection patterns, we projected axonal traces within the 3D masks for each regions across its coronal and sagittal plane. For example, PT^{Fezf2} in parietofrontal nodes both project to the medial regions of caudate putamen (CP), with frontal node to ventromedial region and parietal node to dorsomedial regions (Fig 6c); they did not project to ventral striatum. Within the thalamus, frontal node PT^{Fezf2} project

predominantly to ventromedial regions both in primary and association thalamus while parietal node preferentially target dorsolateral regions in both subregions (Fig. 6d). Within the midbrain, we mainly examined projections across collicular regions and found PT^{Fezf2} from both frontal and parietal nodes specifically target the motor superior colliculus (SCm) with no projections to sensory superior colliculus or inferior colliculus. Within SCm, frontal node PT^{Fezf2} preferentially target ventrolateral regions while parietal node projected to dorsomedial areas. Together, the large set of PT^{Fezf2} subcortical targets may mediate the intention, preparation, and coordinate the execution of tongue and forelimb movements during pellet retrieval and handling. In particular, the thalamic targets of parietofrontal nodes might project back to corresponding cortical regions and support PT^{Fezf2}-mediated cortico-thalamic-cortical pathways, including parietal-frontal communications.

In contrast to PT^{Fezf2}, IT^{PlxnD1} elaborated extensive projections within cerebral cortex and striatum (Fig. 6b, Suppl. Fig. 3a). Within the dorsal cortex, IT^{PlxnD1} in FLA projected strongly to FLP and to contralateral FLA, and IT^{PlxnD1} in FLP project strongly to FLA and to contralateral FLP. Therefore, IT^{PlxnD1} mediate reciprocal connections between ipsilateral FLA-FLP and between bilateral homotypic FLA and FLP (Fig. 6a). In addition, IT^{PlxnD1} from FLA predominantly project to FLP (MOp), lateral secondary motor cortex (MOs), forelimb and nose primary sensory cortex (SSp-n, SSp-ul), secondary sensory cortex (SSs) and visceral areas (VISC). Interestingly, IT^{PlxnD1} in FLP also project to other similar regions targeted by FLA (Fig. 6b). Beyond cortex, IT^{PlxnD1} in FLA and FLP projected strongly to the ventrolateral and mediolateral division of the striatum, respectively (STRd, Fig. 6b). These reciprocal connections between FLA and FLP and their projections to other cortical and striatal targets likely contribute to the concerted activation of bilateral FLA-FLP subnetwork during pellet eating bouts involving coordinated mouth-hand sensorimotor actions. Therefore, as driver lines allow integrated physiological and anatomical analysis of the same PN types, our results begin to uncover the anatomical and connectional basis of functional IT^{PlxnD1} and PT^{Fezf2} subnetworks.

IT^{PlxnD1} and PT^{Fezf2} show distinct spatiotemporal dynamics and spectral properties under ketamine anesthesia

Given the distinct spatiotemporal activation patterns of IT^{PlxnD1} and PT^{Fezf2} in wakeful resting states and sensorimotor behaviors, we further explored whether they differ in network dynamics in a dissociation-like brain state (Vesuna et al., 2020; Whitesell et al., 2021), under ketamine/xylazine anesthesia. We first sampled the temporal activity patterns across 6 different regions of dorsal cortex and found that both cell types showed robust oscillatory activity, with IT^{PlxnD1} displaying faster dynamics than PT^{Fezf2} (Fig. 7a). Quantification of the spectrograms and relative power spectral densities across cortical regions show that IT^{PlxnD1} exhibited oscillations at approximately 1-1.4 Hz while PT^{Fezf2} fluctuated at 0.6-0.9 Hz (Fig. 7b-d).

To visualize a map of cortical regions strongly oscillating at these frequencies, we computed a map of normalized averaged power between 0.6-0.9 and 1-1.4 Hz for each pixel (methods. While IT^{PlxnD1} was strongly active within the frontolateral and posterolateral regions, PT^{Fezf2} was predominantly active in the retrosplenial regions across both frequency bands (Fig. 7e). Furthermore, these two PN types

manifested distinct spatial dynamics across the dorsal cortex, which was visualized by generating a space time plot displaying activity from pixels obtained across a slice of the cortical surface (methods, Fig. 7f). While IT^{PlxnD1} displayed complex spatiotemporal patterns with activities spreading, for example, from central regions to anterolateral and posteromedial or from posteromedial to anterolateral and back, PT^{Fezf2} activities predominantly originated from retrosplenial regions and spread to anterolateral regions (Fig. 7f, Suppl. Videos 6,7). To identify the most dominant spatial activation pattern, we performed seqNMF (MacDowell and Buschman, 2020; Mackevicius et al., 2019) on the activity data and found that the top dimension accounted for more than 80 % of the variance in IT^{PlxnD1} and over 90% in PT^{Fezf2}. Furthermore, we found significant differences in the spatial propagation of activities between the two cell types: whereas IT^{PlxnD1} activities spread multi-directions across most of the dorsal cortex, PT^{Fezf2} activities mainly propagated from retrosplenial toward the frontolateral regions (Fig. 7g). These results show that even under unconstrained brain state such as during anesthesia, IT^{PlxnD1} and PT^{Fezf2} subnetworks operate with distinct spatiotemporal dynamics and spectral properties, likely reflecting their differences in biophysical (Shepherd 2013), physiological (Shepherd 2013), and connectional (e.g. Fig 6) properties.

Discussion

The quest for cellular basis of cerebral cortex architecture has been fueled as well as limited by successive waves of technical advances over the past century. Whereas early cytoarchitectonic analyses of cell distribution patterns identified numerous cortical areas (Brodmann, 1909) and characteristic laminar organization across different areas (Vogt and Vogt, 1919; von Economo and Koskinas, 1925), single cell physiological recording was key to reveal the vertical groupings of neuronal receptive field properties, though initially in anesthetized cortex (Hubel and Wiesel, 1963; Mountcastle et al., 1957). Since its formulation, columnar configuration as the basic units of cortical organization has been a foundational concept that inspired and guided decades of research to unravel its cellular and circuitry underpinnings (Hubel David and Wiesel Torsten, 2005); yet to date the anatomic basis as well as functional significance of “cortical columns” remain elusive and contentious (Adams and Horton, 2003; da Costa and Martin, 2010; Rakic, 2008). Multi-cellular recordings and computational simulation of neural connectivity led to the hypothesis of a “canonical circuit” template, which may perform similar operations common across cortical areas (Douglas and Martin, 1991, 2007; Harris and Shepherd, 2015; Markram et al., 2015); but the concrete cellular basis of “canonical circuit” and its relationship to global cortical networks remain unsolved and largely unexplored. An enduring challenge for understanding cortical architecture is its neuronal diversity and wiring complexity across levels and scales (Engel et al., 2021). Meeting this challenge requires methods to monitor and interpret neural activity patterns across multiple layers and large swaths of cortical territory yet with cell type resolution in real time and in behaving animals. The increasing recognition of and experimental access to diverse neuron types, groups of cells with similar molecular, anatomical, and physiological properties, as neural circuit elements is facilitating contemporary explorations of cortical organization (Huang, 2014). Here, we leverage recent technical advances combining genetic targeting of major PN types with cortex-wide imaging of their spatiotemporal dynamics in behaving mice. We discovered that

genetic and projection defined PN types contribute to distinct and partially parallel subnetworks of cortical processing during a range of brain states and sensorimotor behaviors. These results call for a major revision in our conception of cortical architecture substantially shaped by the concept of columnar organization (da Costa and Martin, 2010); they suggest that dynamic areal and PN type-specific subnetworks is a key feature of cortical functional architecture that integrates across nested levels from microcircuit components to global brain networks. It is possible that columnar information flow between IT and PT, thus the functional integration of corresponding subnetworks, might be dynamically gated by inhibitory and modulatory mechanisms according to brain states and behavioral demand.

Although widefield calcium imaging in rodent cortex provide an opportunity to bridge cellular and cortex-wide measurement of neural activity (Cardin et al., 2020), realizing the full potential of this approach relies on the ability to resolve and access distinct and biologically relevant neuronal types and subpopulations. To date, most if not all these studies examined subpopulation (e.g. those defined by Thy1 and Rbp4 transgenic lines) comprising mixtures of different projection classes (Kauvar et al., 2020; Ma et al., 2016; Vesuna et al., 2020; Xiao et al., 2017), thus have yet to resolve and compare distinct PN projection types and to link anatomical connectivity with functional dynamics in cortical network operations. We have recently established genetic tools for dissecting the hierarchical organization PyN subpopulations based on their molecular genetic programs; these tools enable accessing biologically significant PyN subpopulations through their inherent developmental, anatomical and physiological properties, i.e. “carving nature at its joints”. Among diverse PN types, IT and PT represent two major top-level classes that mediate intracortical processing and subcortical output channels, respectively. Decades of studies have demonstrated their distinct gene expression profiles and programs (Arlotta et al., 2005; Tasic et al., 2018), developmental trajectories (Greig et al., 2013), morphological and connectivity features (Hooks, 2017; Shepherd, 2013), biophysical and physiological properties (Shepherd, 2013), and functional specializations in specific cortical areas and behavior (Li et al., 2015; Takahashi et al., 2020; Tang and Higley, 2020). Here we demonstrate that IT^{PlxnD1} and PT^{Fezf2} operate in separate and partially parallel subnetworks during a range of brain states and sensorimotor behaviors. These results begin to extend the concept of major neuron types linking molecular, developmental, and anatomical features to systems and functional level descriptions. Reliable experimental access to these PN types will facilitate a multi-faceted analysis to integrate cross-level mechanistic explanations that elucidate the nested level of cortical circuit architecture.

Studies in primates and rodents have shown that the posterior parietal cortex (PPC) is a major associational hub that receives inputs from virtually all sensory modalities and frontal motor areas, and supports a variety of functions including sensorimotor transformation, decision making, and movement planning (Carandini and Churchland, 2013; Lyamzin and Benucci, 2019; Whitlock, 2017). In particular, PPC subdivisions are strongly connected with frontal secondary motor cortex in a topographically organized manner (Hovde et al., 2019; Olsen et al., 2019), and this reciprocally connected network has been implicated in movement intension, planning, and the conversion of sensory information to motor commands. The cellular basis of parietal-frontal network is not well understood (Andersen and Cui, 2009; Lyamzin and Benucci, 2019). Here we found that sequential and

co-activation of parietal-frontal PT^{Fezf2} neurons are the most prominent and prevalent activity signatures that precede and correlate with tongue, forelimb, and other body part movements. During the hand-assisted pellet feeding task, training mice to eat without hand specifically occludes PT^{Fezf2} parietal activation that normally precedes hand lift. Furthermore, optogenetic inhibition of the frontal node disrupts linking and hand lift, while the same manipulation of the parietal node disrupts the trajectory and coordination of hand-to-mouth movement. Together, these results suggest PT^{Fezf2} as a key component of the parietal-frontal network implicated in sensorimotor transformation and action control. As PT^{Fezf2} neurons do not extend significant intracortical projections, their co-activation in the parietal-frontal network might result from coordinated presynaptic inputs from, for example, a set of IT PNs that communicate between the two areas, or from cortico-thalamic-cortical pathways (Shepherd and Yamawaki, 2021) linking these two areas. Leveraging genetic tools, future PN type-based anterograde, retrograde, and trans-synaptic tracing will reveal the cell type basis of parietal-frontal network. Furthermore, as the topographic connections between parietal and fontal subdivisions appear to correlate with multiple sensory modalities and body axis (Andersen and Cui, 2009; Hovde et al., 2019; Olsen et al., 2019), cellular resolution analysis using two-photon imaging and optogenetically targeted recordings may resolve these topographically organized circuits that mediate different forms of sensorimotor transformation and action control.

While IT^{PlxnD1} neurons show broad and complex activity patterns during several brain states and numerous episodes of sensorimotor behaviors, we discovered a prominent FLP-FLA subnetwork that correlates to a specific aspect of eating involving coordinated mouth and hand movements. Notably, this subnetwork manifest low activity during pellet retrieval and initial hand lift to mouth, when PT^{Fezf2} in the parietal-frontal subnetwork is strongly active, as well as during chewing. While FLP mostly comprises primary sensory areas of the orofacial and forelimb regions, FLP comprises primary and secondary motor areas of these same body parts. The prominent reciprocal IT^{PlxnD1} projections between these two areas and across bilateral FLP-FLA suggest a compelling anatomical basis underlying the concerted activity dynamics of this functional subnetwork. Furthermore, optogenetic inhibition of FLP-FLA resulted in deficits of pellet handling during eating. Together, these results suggest a significant role of the FLP-FLA subnetwork in the sensorimotor coordination of orofacial and forelimb movement during feeding. Systematic cell type-based studies of FLP and FLA may reveal the neural circuit basis underlying oro-manual dexterity for food handling and eating behaviors.

Given the vast diversity of PN types, our focus on IT^{PlxnD1} and PT^{Fezf2} populations in the current study does not achieve a full description of cortical network operations. Indeed, top-level classes further include cortico-thalamic, near-projecting, and layer 6b populations (Tasic et al., 2018); and the IT class alone comprises diverse transcriptomic (Tasic et al., 2018) and projection (Munoz-Castaneda et al., 2021) types that mediate myriad cortical processing streams (Hooks et al., 2018). Although IT^{PlxnD1} represents a major subset, other IT subpopulations remain to be recognized and analyzed using similar approaches. It is possible, for example, that another IT type might feature a direct presynaptic connection to PT^{Fezf2} (e.g. (Harris and Shepherd, 2015; Hooks, 2017) and share a more similar spatiotemporal activity pattern and closer relationship to the PT^{Fezf2} subnetwork. Future studies will leverage emerging genetic tools to more systematically examine additional sets of PN types and

subpopulations, thereby achieving an increasingly more comprehensive view of functional cortical networks. The proper granularity of cell type targeting need to depend on the question being addressed and match the granularity of behavior and functional readout. Furthermore, simultaneous analysis of two or more PN types in the same animal will be particularly informative in revealing their functional interactions underlying cortical processing. Beyond population level wide-field imaging for identifying cortical areas and subnetworks, cellular resolution studies across spatial scale (e.g. by mesoscope such as COSMOS (Kauvar et al., 2020)) with proper temporal resolution (e.g. targeted electrophysiological recordings (Kvitsiani et al., 2013)) are necessary to decipher the neural circuit basis underlying cortical computation.

Acknowledgments
We thank Joshua Hatfield for performing STP imaging. Katie Matho for advice on analyzing STP imaging datasets. Tatiana Engel and Yanliang Shi for discussions on data analysis. This research was supported NIH grant U19MH114823-01 to Z.J.H. Z.J.H is also supported by a NIH Director's Pioneer Award 1DP1MH129954-01.

Contributions
Z.J.H. and H.M. conceived the project. H.M. built setups, performed experiments and analyzed data. Z.J.H. supervised the research. X.A. provided advice on building feeding behavior setup and provided mice. P.M. provided advice for analyzing neural data. H.K. performed STP viral injections and surgeries. S.Z. performed in situ imaging experiments. S.M. offered advice on building wide-field imaging setup. Z.J.H. and H.M wrote the manuscript.

Note
While this manuscript was in preparation, the following preprint was posted in bioRxiv:
Musall, S., Sun, X.R., Mohan, H., An, X., Gluf, S., Drewes, R., Osten, P., Churchland, A.K. (2021) Pyramidal cell types drive functionally distinct cortical activity patterns during decision-making.
https://www.biorxiv.org/content/10.1101/2021.09.27.461599v2.abstract

Methods

Animals

43 male and female mice were included as part of the study. To express GCaMP6f within specific projection neuron (PN) population, 14 *FezF2-CreER* and 16 *PlexinD1-CreER* knockin mouse lines generated in the lab were crossed with Ai148 (The Jackson Laboratory, Strain #030328), a GCaMP6f reporter line. 3 *VGAT-ChR2-EYFP* (The Jackson Laboratory, Strain #014548) that express the blue light activated opsin ChR2 in GABAergic interneuron population were used for optogentic manipulation. 6 *PlexinD1-CreER* and 4 *FezF2-CreER* crossed with a reporter line expressing LSL-Flp were used for viral expression of flp depended anterograde tracing. Expression of reporters were controlled via the intraperitoneal injection of tamoxifen (20mg/ml) dissolved in corn oil between 1 to 2 months postnatal. All mouse colonies at Cold Spring Harbor Laboratory (CSHL) were maintained in accordance with husbandry protocols approved by the IACUC (Institutional Animal Care and Use Committee) and housed by gender in groups of 2 – 4 with access to food and water *ad libitum* and 12 hour light-dark cycle.

Surgical procedures

For widefield calcium imaging and optogenetic manipulation, adult mice were anesthetized by inhalation of isoflurane maintained between 1-2%. Ketoprofen (5 mg kg−1) was administered subcutaneously as analgesia before and after surgery, and lidocaine (2–4 mg kg−1) was applied intra-incisionally. Mice were mounted in a stereotaxic headframe (Kopf Instruments, 940 series or Leica Biosystems, Angle Two). An incision was made over the scalp to expose the dorsal surface of the skull and the skin pushed aside and fixed in position with tissue adhesive (Vetbond 3M). The surface was cleared using saline and an outer wall was created using dental cement (C&B Metabond, Parkell; Ortho-Jet, Lang Dental) keeping most of the skull exposed. A custom designed circular head plate was implanted using the dental cement to hold it in place. After cleaning the exposed skull thoroughly, a layer of cyanoacrylate (Zap-A-Gap CA+, Pacer Technology) was applied to clear the bone and provide a smooth surface to image calcium activity or for optogenetic stimulation (Musall et al., 2019). For viral injections, we followed the same anesthesia procedure. Under anesthesia, an incision was made over the scalp, a small burr hole drilled in the skull and brain surface exposed. A pulled glass pipette tip of 20–30 μm containing the viral suspension was lowered into the brain; a 300–400 nl volume was delivered at a rate of 30 nl min^{-1} using a Picospritzer (General Valve Corp); the pipette remained in place for 10 min preventing backflow, prior to retraction, after which the incision was closed with 5/0 nylon suture thread (Ethilon Nylon Suture, Ethicon) or Tissueglue (3M Vetbond), and mice were kept warm on a heating pad until complete recovery (Matho et al., 2021).

Viruses

For cell type specific anterograde tracing we injected 400nl of flp dependent viral tracer (AAV2/8-Cag-fDIO TVAeGFP, UNC Vector Core) in *FezF2-CreER;LSL-Flp* mice at either the frontal node (1.85mm Anterior, 0.7mm lateral, 1.25 mm dorsal) or the parietal node (-1.79 to -1.91 mm posterior, 1.25 to 1.35 mm lateral, 0.3-0.7 mm dorsal) and in *PlexinD1-CreER;LSL-Flp* mice at either FLA (1.7

mm anterior, 2.25 mm lateral, 0.3-0.8 mm dorsal) or FLP (0.3mm anterior, 3mm lateral, 0.4-0.8mm dorsal).

Whole-brain STP tomography and image analysis

Whole brain STP imaging was performed as described earlier (Ragan et al., 2012). Briefly, perfused and post fixed brains of adult mice were embedded in 4% oxidized-agarose in 0.05 M PB, cross-linked in 0.2% sodium borohydrate solution (in 0.05 M sodium borate buffer, pH 9.0–9.5).The entire brain was imaged in coronal sections with a 20× Olympus XLUMPLFLN20XW lens (NA 1.0) on a TissueCyte 1000 (Tissuevision) with a Chameleon Ultrafast-2 Ti:Sapphire laser (Coherent) exciting EGFP at 910 nm. Whole-brain image sets were acquired at 0.875 µm x 0.875 µm sampled for 230-270 z sections with a 50 µm z step size. Images were collected by two PMTs (PMT, Hamamatsu, R3896), for signal and autofluorescent background, using a 560-nm dichroic mirror (Chroma, T560LPXR) and band-pass filters (Semrock FF01-680/SP-25). The image tiles were corrected to remove illumination artifacts along the edges and stitched as a grid sequence. Image processing was completed using ImageJ/FIJI and Adobe/Photoshop software with linear level and nonlinear curve adjustments applied only to entire images.

To extract axonal traces, whole brain background images were linearly fit to the imaging channel and regressed out. Background corrected signals were z-scored and a threshold of between 0.5 to 1.5 was set for each brain above which signals were binarized. We used brainreg (Niedworok et al., 2016) (Tyson et al., 2021) to register whole brain data to 10 µm CCFv3 allen map (Wang et al., 2020). To extract volume and peak normalized projection maps (Fig. 6b), we subdivided the whole brain into major nodes as classified by the allen map tree and grouped all regions below that node into the mask of the parent node. We then extracted total axonal count within each roi mask using the binarized data, scaled by the total volume of each mask and normalized by peak value across all nodes. To obtain spatial distribution of axons, 3D masks from registered allen map for each node was used to extract traces specifically enclosed by the roi from binarized data. Average of the projections within mask either along the coronal or sagittal dimension was obtained to extract axonal distribution across each plane. Masks were also projected along these dimensions and the edges used to obtain the borders for each node (Fig. 6c-f). All STP imaging analysis was performed on python 3.

Feeding behavior paradigm

We developed a novel behavior paradigm where in mice use an ethological behavioral sequence to capture, handle and feed on food pellets in a head fixed condition. 2 seconds after trial start, a food pellet (14, 20 or 45 mg, Dustless Precision pellet, F05684, F0071, F0021, Bio-Serv) is delivered on to a custom designed conveyer belt (B375-150XL, Servocity) with a small pellet holder (made of velcro strap with a small hole in center) from an automatic food pellet dispenser (80209-45, Lafayette Instruments) after which a servo motor is uses to rotate the conveyer belt and bring pellet close to the head fixed mouse. The mouse uses its tongue to pick food pellet to its mouth, lift its hand to hold, handle and bite it; bring hands down holding to the remaining pellet; chew and swallow and bring the pellet back again to bite. At the end of 15 seconds after trial start, the conveyer belt rotates back to dispose of any pellet that was not picked and then moves back to starting position under the pellet dispenser.

We began to train mice at least two days after head bar implantation. All mice were older than a month when training was initiated. Mice were first food restricted so that they reach about 85 to 90% of their initial body weight with ad libitum access to water. During food restriction, mice are fed food pellets weighing about 10 to 15% of their body weight. During this period mice were habituated to the setup by head fixing them in increasing durations starting from 10 minutes to 30 minutes over 4 days. After habituation and reaching about 85% of their initial weight, we manually placed food pellets close to its mouth while being head fixed. In the beginning mice pick food with their tongue and try to chew without lifting hands. After a few trials, they begin to lift hands to hold the pellet after picking it with their tongue often within the same session or sometimes after a couple of sessions. Once mice become comfortable in lifting their hands after picking pellet, we begin to deliver the pellet close to mouse automatically by moving the conveyer belt from the pellet dispenser. Most mice learn to perform the task within a week of initiating training. In each session mice consumed about 20 to 80 pellets depending on their body weight and duration of the task. As days progress, mice tend to eat more pellets. At the end of every session, irrespective of the quantity they consume during the task, we provide food pellets of about 10 to 15% of their body weight. We constantly measure the mouse weight and make sure they are always above 85% of their initial weight. As they get better, they perform greater trails even if their weight is at 90 % of initial body weight.

Behavior tracking and classification

Using two high speed cameras (FL3-U3-13S2C-CS, Teledyne FLIR) fitted with varifocal lens (#COT10Z0513CS, B&H), we recorded behavior from both the front and left side of the mouse at 100 frames per second as they performed the task under UV illumination. We used deeplabcut (Mathis et al., 2018) to track a range of task components and body parts from both angles including the pellet, pellet holder, left wrist, lower lip, upperlip, nose, tongue tip, left three fingers and right three fingers (only front the front view). We developed custom algorithms to use these tracked features to identify and classify different behavior events. To identify onset of lick bouts, we calculated spectrogram of the tongue trajectory and extracted the time varying mean power between 4 to 10 Hz. Using a predefined threshold, we obtained the time stamps associated with power rising above threshold and falling below it to obtain the onset and offset times of a lick bout. The onset time of the first lick bout after pellet is delivered to the pellet holder was considered as the lick onset time. The time point when food pellet first crossed the lower lip for at least 100 ms was considered as the pellet in mouth onset time. To obtain hand lift onset time, we used left hand trajectory to identify time point when absolute velocity crossed a predefined threshold. To identify episodes of food handling, we built a long short term memory (LSTM) neural network classifier with 100 hidden units using MATLAB neural network tool box. After manually labelling time stamps associated with food handling for a few example trials across mice, we used these binary time stamps as the dependent variable and all normalized trajectories from the front view of mice as independent variable to train an LSTM classifier. We then used this classifier to extract time stamps associated food handling for the remaining trials. To extract chew episodes, we computed spectrogram of the lower lip trajectory to obtain mean power between 4 to 7 Hz and used 0.1 times the standard deviation of this signal as

the threshold above which events were classified as chewing. Only episodes greater than 0.5 seconds were used.

Wide-field calcium imaging

We used wide field imaging to simultaneously measure GCaMP6f activity across the dorsal cortex. The imaging system used was as described previously (Musall et al., 2019). Briefly, we used a sCMOS (edge 5.5, PCO) camera in combination with a 105 mm focal length top lens (DC-Nikkor, Nikon) and 85 mm (85M-S, Rokinon) bottom lens resulting in a x1.24 magnification and a field of view of about 12.5 x 10.5 mm^2 with an image resolution of 640 x 540 pixels (about 20 µm per pixel dimension) after 4x spatial binning. Images were acquired at 60 Hz alternating between blue (470 nm collimated LED, M470L3, Thorlabs) and violet (405 nm collimated LED, M405L3, Thorlabs) excitation through the same excitation path with the help of a dichroic mirror (no. 87–063, Edmund optics) between the two paths and a 495 nm long pass dichroic (T495lpxr, Chroma) to project both LEDs onto cortical surface. A 525 nm band-pass filter (no. 86–963, Edmund optics) was placed between the camera and lenses to filter GCaMP emission signal. We used the signal associated with 405 nm excitation to regress out the non-calcium dependent hemodynamic signal and isolate the true calcium dependent signal from the 470 nm excitation as described previously ((Allen et al., 2017)Willian E Allen et al 2017 Neuron). This resulting imaging rate of 30 frames per second after hemodynamic correction was used for all subsequent analysis of calcium activity. All widefield data were rigidly aligned to the Allen CCFv3 dorsal map using four anatomical landmarks; the left, center and right edges of the anterior ridge between the frontal cortex and the olfactory bulb and the lambda (Musall et al., 2019; Wang et al., 2020) there by allowing data to be combined across mice and sessions.

Optogenetic Manipulation

To disrupt cortical activity during behavior, we built a laser scanning system that can direct laser stimulation unilaterally or bilaterally across the whole dorsal cortex surface. A collimated beam of blue light (470 nm) from a laser (SSL-473-0100-10TN-D-LED, Sanctity Laser) was fed into a 2D galvo system (GVS 002, Thorlabs) that was directed onto cortical surface using dichroic filters and custom written tool boxes. The system also contained an additional path to simultaneously visualize the cortical surface using a camera (BFS-U3-16S2C-CS, TELEDYNE FLIR). Using this system, we directed blue light with a beam diameter of 400 µm (full width half maximum) bilaterally at 30 Hz. We bilaterally inhibited cortical areas identified from regions active during the feeding behavior task: FLA (1.6 mm anterior, 2.3 mm lateral), FLP(0.5mm anterior, 3.5 mm lateral), Frontal (2 mm anterior, 1 mm lateral) and Parietal (-1.2 mm posterior, 1.2 mm lateral). Obtaining the median onset times associated with lick, PIM and hand lift from previous behavior trials, we randomly turned on the stimulation prior to median lick onset time or during licking or after lick onset but just prior to median pellet in mouth onset time or after pellet in mouth onset but prior to median hand lift onset time or after hand lift onset time while bilaterally inhibiting each of the four ROIs. The inhibition was randomly turned on between control trials where we did not provide any laser stimulation.

Neural and behavior data analysis

All neural and behavior analysis was performed on MATLAB v2018b.

Wakeful resting state analysis

Mice were first habituated to the setup. We imaged and extracted calcium dynamics at 30 fps (as described earlier) across the dorsal cortex for 3 minutes from 6 mice for each PN on two consecutive days. We also simultaneously video recorded behavior at 20 fps. We band pass filtered the calcium activity between 0.01Hz and 5 Hz per pixel to remove the extremely low frequency fluctuations and high frequency noise. Since most of the calcium activity was well below 5 Hz we also band pass filtered behavior videos between 0.01 and 5 Hz to retain the low frequency components of movements. To obtain time varying behavior variance signal, we computed the differential for each pixel in a video frame across time to obtain the motion energy (Stringer et al., 2019) and then computed variance for each frame of the motion energy video (Fig. 1c black trace). We resampled these traces to match sampling rate of calcium activity using resample function in MATLAB. Time points when behavior variance exceeded 0.2 times the standard deviation were classified as active periods and remaining as quiescent. We then split calcium activity videos into active and quiescent episodes based on these time stamps and extracted the variance per pixel across time for each episode to obtain variance maps. We then peak normalized the maps and averaged them across mice and sessions. To compute the neural variance explained by spontaneous behavior, we performed singular value decomposition (SVD) of both calcium activity and motion energy videos and extracted the top 200 temporal components ($S*V^T$) from each decomposition. We then extracted amplitudes of the motion energy temporal components by computing the absolute value of their Hilbert transforms. We then built a liner encoding model using these 200 amplitude signals as independent variables to explain the top 200 temporal components of the calcium activity. We then performed 5 fold cross validation of the model to obtain the cross validated R^2 (Stringer et al., 2019). To compute the variance explained by each body part, we first defined a window around each body part and extracted motion energy within those windows as described earlier. We then extracted variance per frame from each window obtaining a single time varying variance signal associated with each body part. We built a linear model using the z-scored variances per body part as independent variables to explain the top 200 SVD temporal components of calcium activity. We performed 5 fold cross validation to obtain the R^2 associated with each body part. For both linear encoding models we used ridge regression and identified the optimal lambda for each session from a range of values using 5 fold cross validation. To obtain the spatial map of regression weights, we computed the dot product between the model regression weights associated with each body part and the corresponding top 200 SVD spatial components (U) and transformed the resulting vector to a 2D matrix aligning with calcium activity frame.

Sensory stimulation analysis

Before stimulation, mice were injected with chlorprothixene (1 mg/Kg i.p.) and maintained under light isoflurane anesthesia (0.8-1% with O_2). We then placed a custom designed cardboard attached to two piezo actuators (BA5010, PeizoDrive) close to left whisker pad between whiskers and just below the upper and lower lip. We also placed an orange LED close to dorsal region of the left eye. We used an Arduino Uno Rev3 (A00006, Arduino) to drive the piezo and LED. A single trial

consisted of 3 seconds baseline followed by whisker stimulation at 25 Hz for 1 second, 3 second delay, orofacial stimulation at 25 Hz for 1 second, 3 second delay, blinking visual stimulus at about 16 Hz for 1 second followed by an additional 3 seconds before starting the next trial. We recorded one session per day consisting of 20 trials. To extract temporal traces, we used spatial maps obtained by averaging IT^{PlxnD1} activity in response to each sensory stimulation. We identified centers of peak activity in each map and used a circular window of 560 µm diameter to extract signals within the circular mask and average them per frame.

Feeding behavior analysis

To identify the sequential activation pattern during the feeding behavior, we extracted frames one second before and one second after pellet in mouth onset for all trials across mice and sessions. Since each frame is registered to the allen CCFv3, we computed mean for each pixel at every sampling point to obtain an average activation map at each time point centered around pellet in mouth.
To identify cortical areas associated with specific behavior event, we used a linear modelling approach. We generated binary time stamps associated with each behavior event as independent variables. For a single trial the lick variable consisted of 'ones' 0.3 seconds before lick onset to the start of pellet in mouth onset and 'zeros' at all other time points. The pellet in mouth variable consisted of 'ones' from start of pim onset to hand lift onset and 'zeros' everywhere else. The hand lift variable consisted of 'ones' from start of hand lift onset to 0.5 seconds after and 'zeroes' everywhere else. The handling and chew variables similarly contained 'ones' at time stamps classified by handling and chew classifier previously described. We then concatenated these variables vertically across trials within a session to generate the independent variable matrix. We then combined the calcium activity across trials within a session and performed SVD to obtain top 200 temporal components ($S*V^T$) and used a linear model to fit the independent behavior variables to the SVD temporal components obtained from neural activity. We then computed a dot product between the regression weights obtain from the model for each behavior variable and spatial components (U) of the neural activity SVD to transform the regression weights into a spatial map of regions associated with each behavior event.

To identify the center of activation so as to extract temporal traces, we first calculated the average activity per pixel for 1 second before to 2 seconds after pim onset across mice and sessions (Fig. 3a,d). We then applied a mask containing the mouth and nose cortical region over the IT^{PlxnD1} activation map and identified center of peak activation and used it as the center of FLP. Similarly we used MOs and MOp mask to identify the center of FLP. We used MOs mask over the PT^{Fezf2} activation map to identify the center of frontal node and a few cortical regions in the posterior area to identify the center of parietal node.

To extract peak rate of change, we first smoothened raw calcium activity signals centered to either lick onset for PT^{Fezf2} activity in the parietal and frontal node or centered to PIM onset for IT^{PlxnD1} activity in FLA and FLP using a 3rd order Savitzky-Golay (sgolayfilt) filter in MATLAB with a frame length parameter of 7. We then computed its first differential and extracted the peak value between 1

second before to start of lick onset for PT^{Fezf2} activity in parietofrontal nodes and from 0.1 second before to 0.1 second after PIM onset for IT^{PlxnD1} activity in the frontolateral nodes.
To identify distinct activation clusters using Linear Discriminant Analysis (LDA), we first combined temporal activity centered to PIM onset from all trials within an ROI from both PNs along the temporal dimension. We then concatenated the PN type class labels associated with each trial and performed LDA on the activity matrix and class labels using the LDA toolbox (Dwinnell, 2021). (LDA: Linear Discriminant Analysis (https://www.mathworks.com/matlabcentral/fileexchange/29673-lda-linear-discriminant-analysis), MATLAB Central File Exchange. Retrieved December 28, 2021.). We then projected the temporal activity matrix on the first two dimensions identified by the analysis and colored them based on PN type to visualize clusters.

Ketamine anesthetized state analysis

To measure cortical dynamics under anesthesia we injected a mixture of ketamine (87.5 $mgKg^{-1}$) / Xylazine (12.5 $mgKg^{-1}$) i.p. in each mouse and measure activity for 3 minutes at 30 Hz. We used a 560 µm diameter circular mask and extracted average activity per frame within the mask across time to obtain signals from specific regions. We used the chornux (Bokil et al., 2010) toolbox to calculate multi-taper spectrograms and relative power spectral densities. To obtain space time plot (Fig. 7f), we extracted pixels across a one dimensional slice of cortical surface and visualized calcium dynamics for each pixel in the slice across time.

To visualize the most dominant spatial activation pattern, we used seqNMF as described previously (MacDowell and Buschman, 2020; Mackevicius et al., 2019). Briefly, the calcium activity was first band pass filtered between 0.01 Hz and 5 Hz. Since seqNMF is applied to non-negative matrices, values below 0 were set to 0. This 3D matrix is transformed to a 2D matrix of pixels x time and seqNMF with parameters sequence length: 30 (1 second), number of dimensions: 10 and lambda: 0.01 was used to obtain the most dominant sequence. Across a range of lambda values seqNMF identified just one sequence for both IT^{PlxnD1} and PT^{Fezf2} accounting for greater than 80% of variance.

References

Adams, D.L., and Horton, J.C. (2003). Capricious expression of cortical columns in the primate brain. Nat Neurosci *6*, 113-114.

Allen, W.E., Kauvar, I.V., Chen, M.Z., Richman, E.B., Yang, S.J., Chan, K., Gradinaru, V., Deverman, B.E., Luo, L., and Deisseroth, K. (2017). Global Representations of Goal-Directed Behavior in Distinct Cell Types of Mouse Neocortex. Neuron *94*, 891-907 e896.

Andersen, R.A., and Cui, H. (2009). Intention, action planning, and decision making in parietal-frontal circuits. Neuron *63*, 568-583.

Arlotta, P., Molyneaux, B.J., Chen, J., Inoue, J., Kominami, R., and Macklis, J.D. (2005). Neuronal subtype-specific genes that control corticospinal motor neuron development in vivo. Neuron *45*, 207-221.

Bokil, H., Andrews, P., Kulkarni, J.E., Mehta, S., and Mitra, P.P. (2010). Chronux: a platform for analyzing neural signals. J Neurosci Methods *192*, 146-151.

Bota, M., Sporns, O., and Swanson, L.W. (2015). Architecture of the cerebral cortical association connectome underlying cognition. Proc Natl Acad Sci U S A *112*, E2093-2101.

Brodmann, K. (1909). Vergleichende Lokalisationslehre der Grosshirnrinde in ihren Prinzipien dargestellt auf Grund des Zellenbaues (Barth).

Carandini, M., and Churchland, A.K. (2013). Probing perceptual decisions in rodents. Nat Neurosci *16*, 824-831.

Cardin, J.A., Crair, M.C., and Higley, M.J. (2020). Mesoscopic Imaging: Shining a Wide Light on Large-Scale Neural Dynamics. Neuron *108*, 33-43.

da Costa, N.M., and Martin, K.A. (2010). Whose Cortical Column Would that Be? Front Neuroanat *4*, 16.

Douglas, R.J., and Martin, K.A. (1991). A functional microcircuit for cat visual cortex. J Physiol *440*, 735-769.

Douglas, R.J., and Martin, K.A. (2007). Mapping the matrix: the ways of neocortex. Neuron *56*, 226-238.

Engel, T.A., Scholvinck, M.L., and Lewis, C.M. (2021). The diversity and specificity of functional connectivity across spatial and temporal scales. Neuroimage *245*, 118692.

Gamanut, R., Kennedy, H., Toroczkai, Z., Ercsey-Ravasz, M., Van Essen, D.C., Knoblauch, K., and Burkhalter, A. (2018). The Mouse Cortical Connectome, Characterized by an Ultra-Dense Cortical Graph, Maintains Specificity by Distinct Connectivity Profiles. Neuron *97*, 698-715 e610.

Gilad, A., Gallero-Salas, Y., Groos, D., and Helmchen, F. (2018). Behavioral Strategy Determines Frontal or Posterior Location of Short-Term Memory in Neocortex. Neuron *99*, 814-828 e817.

Gozzi, A., and Schwarz, A.J. (2016). Large-scale functional connectivity networks in the rodent brain. Neuroimage *127*, 496-509.

Greig, L.C., Woodworth, M.B., Galazo, M.J., Padmanabhan, H., and Macklis, J.D. (2013). Molecular logic of neocortical projection neuron specification, development and diversity. Nat Rev Neurosci *14*, 755-769.

Harris, J.A., Mihalas, S., Hirokawa, K.E., Whitesell, J.D., Choi, H., Bernard, A., Bohn, P., Caldejon, S., Casal, L., Cho, A., *et al.* (2019). Hierarchical organization of cortical and thalamic connectivity. Nature *575*, 195-202.

Harris, K.D., and Shepherd, G.M. (2015). The neocortical circuit: themes and variations. Nat Neurosci *18*, 170-181.

Hooks, B.M. (2017). Sensorimotor Convergence in Circuitry of the Motor Cortex. Neuroscientist *23*, 251-263.

Hooks, B.M., Papale, A.E., Paletzki, R.F., Feroze, M.W., Eastwood, B.S., Couey, J.J., Winnubst, J., Chandrashekar, J., and Gerfen, C.R. (2018). Topographic precision in sensory and motor corticostriatal projections varies across cell type and cortical area. Nat Commun *9*, 3549.

Hovde, K., Gianatti, M., Witter, M.P., and Whitlock, J.R. (2019). Architecture and organization of mouse posterior parietal cortex relative to extrastriate areas. Eur J Neurosci *49*, 1313-1329.

Huang, Z.J. (2014). Toward a genetic dissection of cortical circuits in the mouse. Neuron *83*, 1284-1302.

Hubel David, H., and Wiesel Torsten, N. (2005). Brain and visual perception: the story of a 25-year collaboration (New York, NY: Oxford University Press).

Hubel, D.H., and Wiesel, T.N. (1963). Shape and arrangement of columns in cat's striate cortex. J Physiol *165*, 559-568.

Kauvar, I.V., Machado, T.A., Yuen, E., Kochalka, J., Choi, M., Allen, W.E., Wetzstein, G., and Deisseroth, K. (2020). Cortical Observation by Synchronous Multifocal Optical Sampling Reveals Widespread Population Encoding of Actions. Neuron *107*, 351-367 e319.

Kvitsiani, D., Ranade, S., Hangya, B., Taniguchi, H., Huang, J.Z., and Kepecs, A. (2013). Distinct behavioural and network correlates of two interneuron types in prefrontal cortex. Nature *498*, 363-366.

Lerner, T.N., Ye, L., and Deisseroth, K. (2016). Communication in Neural Circuits: Tools, Opportunities, and Challenges. Cell *164*, 1136-1150.

Li, N., Chen, T.W., Guo, Z.V., Gerfen, C.R., and Svoboda, K. (2015). A motor cortex circuit for motor planning and movement. Nature *519*, 51-56.

Lyamzin, D., and Benucci, A. (2019). The mouse posterior parietal cortex: Anatomy and functions. Neurosci Res *140*, 14-22.

Ma, Y., Shaik, M.A., Kozberg, M.G., Kim, S.H., Portes, J.P., Timerman, D., and Hillman, E.M. (2016). Resting-state hemodynamics are spatiotemporally coupled to synchronized and symmetric neural activity in excitatory neurons. Proc Natl Acad Sci U S A *113*, E8463-E8471.

MacDowell, C.J., and Buschman, T.J. (2020). Low-Dimensional Spatiotemporal Dynamics Underlie Cortex-wide Neural Activity. Curr Biol *30*, 2665-2680 e2668.

Mackevicius, E.L., Bahle, A.H., Williams, A.H., Gu, S., Denisenko, N.I., Goldman, M.S., and Fee, M.S. (2019). Unsupervised discovery of temporal sequences in high-dimensional datasets, with applications to neuroscience. Elife *8*.

Markram, H., Muller, E., Ramaswamy, S., Reimann, M.W., Abdellah, M., Sanchez, C.A., Ailamaki, A., Alonso-Nanclares, L., Antille, N., Arsever, S., *et al.* (2015). Reconstruction and Simulation of Neocortical Microcircuitry. Cell *163*, 456-492.

Mathis, A., Mamidanna, P., Cury, K.M., Abe, T., Murthy, V.N., Mathis, M.W., and Bethge, M. (2018). DeepLabCut: markerless pose estimation of user-defined body parts with deep learning. Nat Neurosci *21*, 1281-1289.

Matho, K.S., Huilgol, D., Galbavy, W., He, M., Kim, G., An, X., Lu, J., Wu, P., Di Bella, D.J., Shetty, A.S., *et al.* (2021). Genetic dissection of the glutamatergic neuron system in cerebral cortex. Nature *598*, 182-187.

Mountcastle, V.B., Davies, P.W., and Berman, A.L. (1957). Response properties of neurons of cat's somatic sensory cortex to peripheral stimuli. J Neurophysiol *20*, 374-407.

Munoz-Castaneda, R., Zingg, B., Matho, K.S., Chen, X., Wang, Q., Foster, N.N., Li, A., Narasimhan, A., Hirokawa, K.E., Huo, B., *et al.* (2021). Cellular anatomy of the mouse primary motor cortex. Nature *598*, 159-166.

Musall, S., Kaufman, M.T., Juavinett, A.L., Gluf, S., and Churchland, A.K. (2019). Single-trial neural dynamics are dominated by richly varied movements. Nat Neurosci *22*, 1677-1686.

Niedworok, C.J., Brown, A.P., Jorge Cardoso, M., Osten, P., Ourselin, S., Modat, M., and Margrie, T.W. (2016). aMAP is a validated pipeline for registration and segmentation of high-resolution mouse brain data. Nat Commun *7*, 11879.

Olsen, G.M., Hovde, K., Kondo, H., Sakshaug, T., Somme, H.H., Whitlock, J.R., and Witter, M.P. (2019). Organization of Posterior Parietal-Frontal Connections in the Rat. Front Syst Neurosci *13*, 38.

Ragan, T., Kadiri, L.R., Venkataraju, K.U., Bahlmann, K., Sutin, J., Taranda, J., Arganda-Carreras, I., Kim, Y., Seung, H.S., and Osten, P. (2012). Serial two-photon tomography for automated ex vivo mouse brain imaging. Nat Methods *9*, 255-258.

Rakic, P. (2008). Confusing cortical columns. Proc Natl Acad Sci U S A *105*, 12099-12100.

Shepherd, G.M. (2013). Corticostriatal connectivity and its role in disease. Nat Rev Neurosci *14*, 278-291.

Shepherd, G.M.G., and Yamawaki, N. (2021). Untangling the cortico-thalamo-cortical loop: cellular pieces of a knotty circuit puzzle. Nat Rev Neurosci *22*, 389-406.

Smith, S.M., Vidaurre, D., Beckmann, C.F., Glasser, M.F., Jenkinson, M., Miller, K.L., Nichols, T.E., Robinson, E.C., Salimi-Khorshidi, G., Woolrich, M.W., *et al.* (2013). Functional connectomics from resting-state fMRI. Trends Cogn Sci *17*, 666-682.

Steinmetz, N.A., Aydin, C., Lebedeva, A., Okun, M., Pachitariu, M., Bauza, M., Beau, M., Bhagat, J., Bohm, C., Broux, M., *et al.* (2021). Neuropixels 2.0: A miniaturized high-density probe for stable, long-term brain recordings. Science *372*.

Stringer, C., Pachitariu, M., Steinmetz, N., Reddy, C.B., Carandini, M., and Harris, K.D. (2019). Spontaneous behaviors drive multidimensional, brainwide activity. Science *364*, 255.

Svoboda, K., Helmchen, F., Denk, W., and Tank, D.W. (1999). Spread of dendritic excitation in layer 2/3 pyramidal neurons in rat barrel cortex in vivo. Nat Neurosci *2*, 65-73.

Takahashi, N., Ebner, C., Sigl-Glockner, J., Moberg, S., Nierwetberg, S., and Larkum, M.E. (2020). Active dendritic currents gate descending cortical outputs in perception. Nat Neurosci *23*, 1277-1285.

Tang, L., and Higley, M.J. (2020). Layer 5 Circuits in V1 Differentially Control Visuomotor Behavior. Neuron *105*, 346-354 e345.

Tasic, B., Yao, Z., Graybuck, L.T., Smith, K.A., Nguyen, T.N., Bertagnolli, D., Goldy, J., Garren, E., Economo, M.N., Viswanathan, S., *et al.* (2018). Shared and distinct transcriptomic cell types across neocortical areas. Nature *563*, 72-78.

Tyson, A.L., Vélez-Fort, M., Rousseau, C.V., Cossell, L., Tsitoura, C., Obenhaus, H.A., Claudi, F., Lenzi, S.C., Branco, T., and Margrie, T.W. (2021). Tools for accurate post hoc determination of marker location within whole-brain microscopy images. bioRxiv.

Van Essen, D.C., and Glasser, M.F. (2018). Parcellating Cerebral Cortex: How Invasive Animal Studies Inform Noninvasive Mapmaking in Humans. Neuron *99*, 640-663.

Vesuna, S., Kauvar, I.V., Richman, E., Gore, F., Oskotsky, T., Sava-Segal, C., Luo, L., Malenka, R.C., Henderson, J.M., Nuyujukian, P., *et al.* (2020). Deep posteromedial cortical rhythm in dissociation. Nature *586*, 87-94.

Vogt, C., and Vogt, O. (1919). Allgemeine ergebnisse unserer hirnforschung, Vol 21 (JA Barth). von Economo, C.F., and Koskinas, G.N. (1925). Die cytoarchitektonik der hirnrinde des erwachsenen menschen (J. Springer).

Wang, Q., Ding, S.L., Li, Y., Royall, J., Feng, D., Lesnar, P., Graddis, N., Naeemi, M., Facer, B., Ho, A., *et al.* (2020). The Allen Mouse Brain Common Coordinate Framework: A 3D Reference Atlas. Cell *181*, 936-953 e920.

Wekselblatt, J.B., Flister, E.D., Piscopo, D.M., and Niell, C.M. (2016). Large-scale imaging of cortical dynamics during sensory perception and behavior. J Neurophysiol *115*, 2852-2866.

Whitesell, J.D., Liska, A., Coletta, L., Hirokawa, K.E., Bohn, P., Williford, A., Groblewski, P.A., Graddis, N., Kuan, L., Knox, J.E., *et al.* (2021). Regional, Layer, and Cell-Type-Specific Connectivity of the Mouse Default Mode Network. Neuron *109*, 545-559 e548.

Whitlock, J.R. (2017). Posterior parietal cortex. Curr Biol *27*, R691-R695.

Xiao, D., Vanni, M.P., Mitelut, C.C., Chan, A.W., LeDue, J.M., Xie, Y., Chen, A.C., Swindale, N.V., and Murphy, T.H. (2017). Mapping cortical mesoscopic networks of single spiking cortical or sub-cortical neurons. Elife *6*.

Zingg, B., Hintiryan, H., Gou, L., Song, M.Y., Bay, M., Bienkowski, M.S., Foster, N.N., Yamashita, S., Bowman, I., Toga, A.W., *et al.* (2014). Neural networks of the mouse neocortex. Cell *156*, 1096-1111.

Figure Legends

Figure 1. Distinct cortical activity patterns of IT^{PlxnD1} and PT^{Fezf2} during wakeful resting and upon sensory input

a. Serial two photon tomography images showing distribution of PT^{FezF2} and IT^{PlxnD1} across dorsal cortex in *FezF2-CreER:Ai148* and *PlexinD1-CreER:Ai148* mice. Blue dashed lines indicate approximate transition from layer 1 to layer 2/3 to layer 5a to layer 5b to layer 6.
b. mRNA in situ images and distribution of $Fezf2^+$ (left), $PlexinD1^+$ (middle), and $Satb2^+$ in red and $PlexinD1^+$ in green overlaid (right) cells. Note that $PlexinD1^+$ cells represent a subset of $Satb2^+$ IT cells.
c. Example variance trace of behavior from video recordings (black) and corresponding variance trace of neural activity from IT^{PlxnD1} and PT^{FezF2} from wide-field GCaMP6f imaging. Gray blocks indicate active episodes identified from behavior variance trace.
d. Peak normalized variance maps of spontaneous neural activity during active and quiescent episodes.
e. Distribution of the percentage of cross validated IT^{PlxnD1} and PT^{FezF2} neural activity variance explained by full frame behavior variance obtained from a linear encoding model (12 sessions from 6 mice each, Wilcoxon rank sum test $p < 0.05$).
f. Distribution of the percentage of cross validated IT^{PlxnD1} and PT^{FezF2} neural activity variance explained by variance of specific body part movements obtained from the linear encoding model (12 sessions from 6 mice each, Wilcoxon rank sum test, hands $p < 0.05$).
g. Illustration of unimodal sensory stimulation paradigm.
h. Mean activity maps of IT^{PlxnD1} and PT^{FezF2} in response to corresponding unimodal sensory simulation (average of 12 sessions from 6 mice each).
i. Single trial IT^{PlxnD1} and PT^{FezF2} activity within orofacial, whisker and visual areas during corresponding sensory stimulation.
j. Single trial heat maps of IT^{PlxnD1} and PT^{FezF2} activity from whisker, orofacial and visual cortex in response to corresponding sensory stimulus from 1 example mouse.
k. Mean temporal dynamics of IT^{PlxnD1} and PT^{FezF2} activity in whisker, orofacial and visual cortex in response to corresponding sensory stimulus (average of 12 sessions from 6 mice each, shaded region indicates 2 s.e.m).
l. Distribution of IT^{PlxnD1} and PT^{FezF2} activity intensity in whisker, orofacial and visual cortex in response to corresponding sensory stimulus (Wilcoxon rank sum test, $p<0.0005$ for all conditions).

Figure 1. Supplementary figure 1.

a. Peak normalized variance maps for each mouse (in columns) during quiescent and active episodes averaged over two sessions each.
b. Distribution of standard deviations during quiescent (Q) versus active (A) episodes in IT^{PlxnD1} (blue) and PT^{Fezf2} (green). (Quiescent vs. Active, IT^{PlxnD1} $p < 0.005$ Wilcoxon rank sum test, PT^{Fezf2} $p<0.0005$ Wilcoxon rank sum test, 12 sessions from 6 mice each).
c. Distribution of Pearson's correlation coefficients between quiescent variance maps within IT^{PlxnD1} (blue), PT^{Fezf2} (green) and between IT^{PlxnD1} and PT^{Fezf2} (blue green). *** $p<0.0005$ Wilcoxon rank sum test.

d. Distribution of Pearson's correlation coefficients between active variance maps within IT^{PlxnD1} (blue), PT^{Fezf2} (green) and between IT^{PlxnD1} and PT^{Fezf2} (blue green). *** $p<0.0005$ Wilcoxon rank sum test.
e. IT^{PlxnD1} (top) and PT^{Fezf2} (bottom) regression weight maps associated with hand movements obtained from the linear encoding model. PT^{Fezf2} was most active in parietal area while IT^{PlxnD1} was most active in hind limb sensory area
f. Distribution of IT^{PlxnD1} (blue) and PT^{Fezf2} (green) active variance maps projected to the subspace spanned by the top two principal components.
g. Distribution of IT^{PlxnD1} (blue) and PT^{Fezf2} (green) quiescent variance maps projected to the subspace spanned by the top two principal components.

Figure 1. Supplementary figure 2

a. Mean peak normalized activity maps of IT^{PlxnD1} (top) and PT^{FezF2} (bottom) in response to corresponding unimodal sensory simulation (average of 12 sessions from 6 mice each).
b. Distribution of Pearson's correlation coefficients between sensory activation maps within IT^{PlxnD1} (blue), PT^{Fezf2} (green) and between IT^{PlxnD1} and PT^{Fezf2} (blue green). *** $p<0.0005$, * $p< 0.05$, Wilcoxon rank sum test.

Figure 2. Distinct PT^{Fezf2} and IT^{PlxnD1} subnetworks tuned to different sensorimotor components of a feeding behavior

a. Schematic of the head fixed feeding behavior task.
b. Example traces of tracked body parts and episodes of classified behavior events. Colored lines represent different body parts as indicated. light green shade: handle and eat episodes; orange shade: chewing episode).
c. Mean IT^{PlxnD1} and PT^{FezF2} sequential activity maps during the feeding sequence before and after pellet-in-mouth onset (IT^{PlxnD1} - 23 sessions from 6 mice, PT^{Fezf2} - 24 sessions from 5 mice). Note the largely sequential activation of: 1.left barrel cortex when right whiskers sensed approaching food pellet; 2.forelimb sensory area with limb movements that adjusted grips of hand bar as pellet approaches closer; 3.orofacial sensory areas (FLP) when pellet-in-mouth;4. FLA-FLP on handling and eating the pellet; 5. parietal node while making postural adjustments as pellet arrives; 6. frontal node during lick and 7. parietal node again during hand lift.
d. Spatial maps of IT^{PlxnD1} (top) and PT^{Fezf2} (bottom) regression weights from an encoding model associated with lick, pellet-in-mouth, hand lift, eating and handling, and chewing (IT^{PlxnD1} - 23 sessions from 6 mice, PT^{Fezf2} - 24 sessions from 5 mice).

Figure 3. IT^{PlxnD1} and PT^{FezF2} within frontolateral and parietofrontal nodes show distinct temporal dynamics during feeding behavior

a. Mean overall activity map of PT^{FezF2} across the dorsal cortex during the feeding sequence from 1 second before to 2 seconds after PIM onset (24 sessions from 5 mice).
b. Example single PT^{FezF2} activity traces from FLA (magenta), FLP (orange), frontal (dark brown) and parietal (light brown) nodes during feeding behavior; vertical bars indicate different behavior events.
c. Single trial heat maps of PT^{FezF2} activities from frontal and parietal nodes centered to onset of licking, PIM, and hand lift (5 sessions from one example mouse).

d. Mean overall activity map of IT^{PlxnD1} across the dorsal cortex during the feeding sequence from 1 second before to 2 seconds after PIM onset (23 sessions from 6 mice).
e. Example single IT^{PlxnD1} activity traces from FLA, FLP, frontal and parietal nodes during feeding behavior.
f. Single trial heat maps of IT^{PlxnD1} activities from FLA and FLP nodes centered to onset of licking, PIM and hand lift (5 sessions from one example mouse).
g. Mean PT^{FezF2} activity within frontal and parietal node centered to onset of lick, PIM, and hand lift. Grey dashed lines indicate median onset times of other events relative to centered event (5 sessions from one example mouse, shading around trace 2 s.e.m). Grey shade indicates eating-handling episode.
h. Distribution of peak rate of change of PT^{FezF2} activities from parietal and frontal node centered to lick onset (24 sessions from 5 mice, Wilcoxon rank sum test $p < 0.0005$).
i. Mean IT^{PlxnD1} activity within FLA and FLP centered to onset of lick, PIM, and hand lift; grey dashed lines indicate median onset times of other events relative to centered event (5 sessions from one example mouse, shading around trace 2 s.e.m). Grey shade indicates eating-handling episode.
j. Distribution of peak rate of change of IT^{PlxnD1} activities from FLA and FLP centered to PIM onset (23 sessions from 6 mice, Wilcoxon rank sum test $p < 0.0005$).
k. Single trial heat maps of IT^{PlxnD1} and PT^{FezF2} activities within parietal, frontal, FLP and FLA nodes centered to PIM (IT^{PlxnD1} - 23 sessions from 6 mice, PT^{Fezf2} - 24 sessions from 5 mice).
l. Mean IT^{PlxnD1} and PT^{FezF2} temporal dynamics within parietal (light brown), frontal (dark brown), FLP (Orange) and FLA (Magenta) centered to PIM. Grey dashed lines indicate median onset times of lick and hand lift relative to PIM (IT^{PlxnD1} - 23 sessions from 6 mice, PT^{Fezf2} - 24 sessions from 5 mice, shading around trace 2 s.e.m). Left Inset: Overlaid activity maps of IT^{PlxnD1} (Blue) and PT^{FezF2} (green) after thresholding indicating distinct nodes preferentially active during the feeding sequence.
m. Distribution of IT^{PlxnD1} and PT^{FezF2} activities centered at PIM onset from parietal, frontal, FLP and FLA node and projected to the subspace spanned by the first two linear discriminant analysis dimensions (IT^{PlxnD1} - 23 sessions from 6 mice, PT^{Fezf2} - 24 sessions from 5 mice).

Figure 4. Feeding without hand lift selectively occludes PT^{FezF2} activity in parietal node.

a. Schematic of feeding without hand following preventing hand lift with a blocking plate.
b. Single trial heat maps of PT^{FezF2} activity within frontal and parietal nodes centered to onset of licking and PIM during feeding without hand lift (2 sessions from one example mouse).
c. Mean PT^{FezF2} activity within parietal (light green) and frontal (dark green) nodes centered to onset of lick, PIM during feeding without hand (left and middle panels; 2 sessions from one example mouse, shading around trace 2 s.e.m), and PIM during feeding with hand (right, 5 sessions from the same mouse, shading around trace 2 s.e.m).
d. Single trial heat maps of IT^{PlxnD1} activity within FLA and FLP centered to onset of licking and PIM during feeding without hand (3 sessions from one example mouse).
e. Mean IT^{PlxnD1} activity within FLA and FLP centered to onset of licking, PIM during the feeding without hand, (left and middle panels; 3 sessions from one example mouse, shading around trace 2 s.e.m), and PIM during feeding with hand (right, 5 sessions from the same mouse, shading around trace 2 s.e.m).

f. Distribution of PT^{FezF2} activity intensity during 1 sec post PIM onset from parietal and frontal nodes across behaviors with and without hand (no lift: 13 sessions from 5 mice, lift: 24 sessions from the same 5 mice, lift vs. no lift in parietal node $p < 0.0005$, Wilcoxon rank sum test).
g. Distribution of IT^{PlxnD1} activity intensity during 1 sec post PIM onset from FLA and FLP across behaviors with and without hand (no lift: 15 sessions from 6 mice, lift: 23 sessions from the same 6 mice, lift vs. no lift in FLA $p < 0.0005$, Wilcoxon rank sum test).
h. Mean PT^{FezF2} (top) and IT^{PlxnD1} (bottom) spatial activity maps during 1 second post PIM onset for behaviors with (left) and without (right) hand.
i. Difference in PT^{FezF2} (top) and IT^{PlxnD1} (bottom) mean spatial activity maps between behaviors with and without hand.

Figure 5. Inhibition of Parietofrontal and frontolateral subnetworks differentially disrupts sensorimotor components of feeding behavior

a. Schematic of optogenetic laser scanning setup.
b. Single trial (translucent) and averaged (opaque) tongue trajectories centered to bilateral inhibition (bottom row) of frontal (dark brown), parietal (light brown) and frontolateral (magenta, pooled across FLA and FLP) nodes. Grey trajectories (top row) are from control trials preceding inhibition trials (n = 3 mice).
c. Distribution of mean tongue length before and during inhibition of frontal (dark brown, $p < 0.005$ wilcoxon sign rank test), parietal (light brown) and frontolateral (magenta, $p < 0.0005$ Wilcoxon sign rank test) nodes.
d. Distribution of durations to lick pellet after trial start during control trials versus inhibition of frontal ($p < 0.005$, Wilcoxon rank sum test), parietal, and frontolateral ($p < 0.0005$, Wilcoxon rank sum test) nodes.
e. Probability of hand lift during inhibition of frontal ($p<0.0005$, chi-square test), parietal and frontolateral ($p<0.0005$, chi-square test) nodes compared to control.
f. Mean vertical hand trajectory from side view (top, shading around trace 2 s.e.m) and absolute velocity (bottom, shading around trace 2 s.e.m) while lifting hand to mouth during control (black) and inhibition of frontal (dark brown), parietal (light brown) and frontolateral (magenta) nodes. Notice widening of velocity signal during parietal inhibition.
g. Distribution of the integral of absolute velocity signal for 1 second post hand lift during control and inhibition of frontal (dark brown), parietal (light brown, $p<0.005$ Wilcoxon rank sum test) and frontolateral (magenta) nodes.
h. Mean normalized vertical trajectory of left finger from the front view after licking pellet into mouth during control trials (black, shading around trace 2 s.e.m) and inhibition of frontal (dark brown), parietal (light brown) and frontolateral (magenta) nodes.
i. Distribution of mean normalized finger to mouth distance during control versus inhibition of frontal (dark brown, $p<0.0005$ wilcoxon rank sum test), parietal (light brown, $p<0.05$ Wilcoxon rank sum test) and frontolateral (magenta, $p<0.0005$ Wilcoxon rank sum test) nodes.
j. Distribution of number of secondary hand lifts during control versus inhibition of frontal (dark brown, $p<0.0005$ wilcoxon rank sum test), parietal (light brown, $p<0.05$ Wilcoxon rank sum test) and frontolateral (magenta, $p<0.0005$ Wilcoxon rank sum test) nodes.

k. Distribution of duration of hand held close to mouth during control versus inhibition of frontal (dark brown, $p<0.0005$ wilcoxon rank sum test), parietal (light brown, $p<0.005$ Wilcoxon rank sum test) and frontolateral (magenta, $p<0.0005$ Wilcoxon rank sum test) nodes.
l. Example horizontal trajectory of the left fingers during control and inhibition of the frontolateral node.
m. Distribution of the number of horizontal pellet grasp-release movements during control versus inhibition of frontal (dark brown, $p<0.05$ wilcoxon rank sum test), parietal (light brown) and frontolateral (magenta, $p<0.0005$ Wilcoxon rank sum test) nodes.

Figure 6. Brain wide projections of IT^{PlxnD1} and PT^{FezF2} from frontolateral and parietofrontal networks.

a. Anterograde projections of IT^{PlxnD1} from FLA and FLP and PT^{FezF2} from frontal and parietal nodes within isocortex projected to the dorsal cortical surface from an example mouse.
b. Brain-wide volume and peak normalized projection intensity maps of IT^{PlxnD1} from FLA and FLP and PT^{FezF2} from frontal and parietal nodes from an example mouse. Black font indicates injection site; larger gray font indicate regions with significant projections; smaller gray font indicate regions analyzed.
c. Spatial distribution of axonal projections of IT^{PlxnD1} from FLA and FLP (top) and PT^{Fezf2} parietal and frontal nodes (bottom) within the striatum projected onto the coronal and sagittal plane.
d. Spatial distribution of axonal projections of PT^{Fezf2} from parietal and frontal nodes within the primary and association thalamus projected onto the coronal and sagittal plane.
e. Spatial distribution of axonal projections of PT^{Fezf2} from parietal and frontal nodes within the motor Superior colliculus (SCm, magenta), sensory superior colliculus (SCs, yellow) and inferior colliculus (IC, brown) projected onto the coronal and sagittal plane.
f. Spatial distribution of axonal projections of PT^{Fezf2} from parietal and frontal nodes (bottom) within the hindbrain projected onto the coronal and sagittal plane.

Figure 6. Supplementary figure 3

a. Three dimensional rendering of axonal projections of IT^{PlxnD1} from FLA and FLP and PT^{Fezf2} from Frontal and Parietal node. Yellow circle indicates injection site.

Figure 7. IT^{PlxnD1} and PT^{FezF2} show distinct spatiotemporal dynamics and spectral properties under ketamine anesthesia.

a. Example single trial traces of IT^{PlxnD1} and PT^{FezF2} activities from 6 different cortical areas during ketamine/xylazine anesthesia. Colors represent cortical areas as indicated (VC- primary visual Cortex, RSp- medial retrosplenial cortex, HL – primary hindlimb sensory cortex, MOs – secondary motor Cortex, MOp – primary motor cortex, BC – barrel cortex).
b. Example spectrogram of IT^{PlxnD1} and PT^{FezF2} activity from MOp and RSp of one mouse.
c. Mean relative power spectral density of IT^{PlxnD1} (blue) and PT^{FezF2} (green) activity from MOp and RSp (18 sessions across 6 mice, shading around trace 2 s.e.m).
d. Distribution of average relative power within MOp and RSp of IT^{PlxnD1} and PT^{FezF2} between 0.6–0.9 Hz and 1–1.4 Hz (MOp 1-1.4Hz IT^{PlxnD1} vs. PT^{FezF2} $p < 0.0005$; RSp 0.6–0.9 Hz and 1-1.4 Hz IT^{PlxnD1} vs. PT^{FezF2} $p<0.05$, Wilcoxon rank sum test).
e. Spatial distribution of average relative power between 0.6–0.9 Hz and 1–1.4 Hz from IT^{PlxnD1} (top) and PT^{FezF2} (bottom, 18 sessions across 6 mice).

f. Example space time plots of the neural activity across a slice of the dorsal cortex (red dashed lines) from IT^{PlxnD1} (top) and PT^{FezF2} (bottom). Middle, zoomed-in activity from indicated top and bottom panels.
g. Example activation sequence of the most dominant pattern (1st dimension) identified by seqNMF from IT^{PlxnD1} (top) and PT^{FezF2} (bottom).

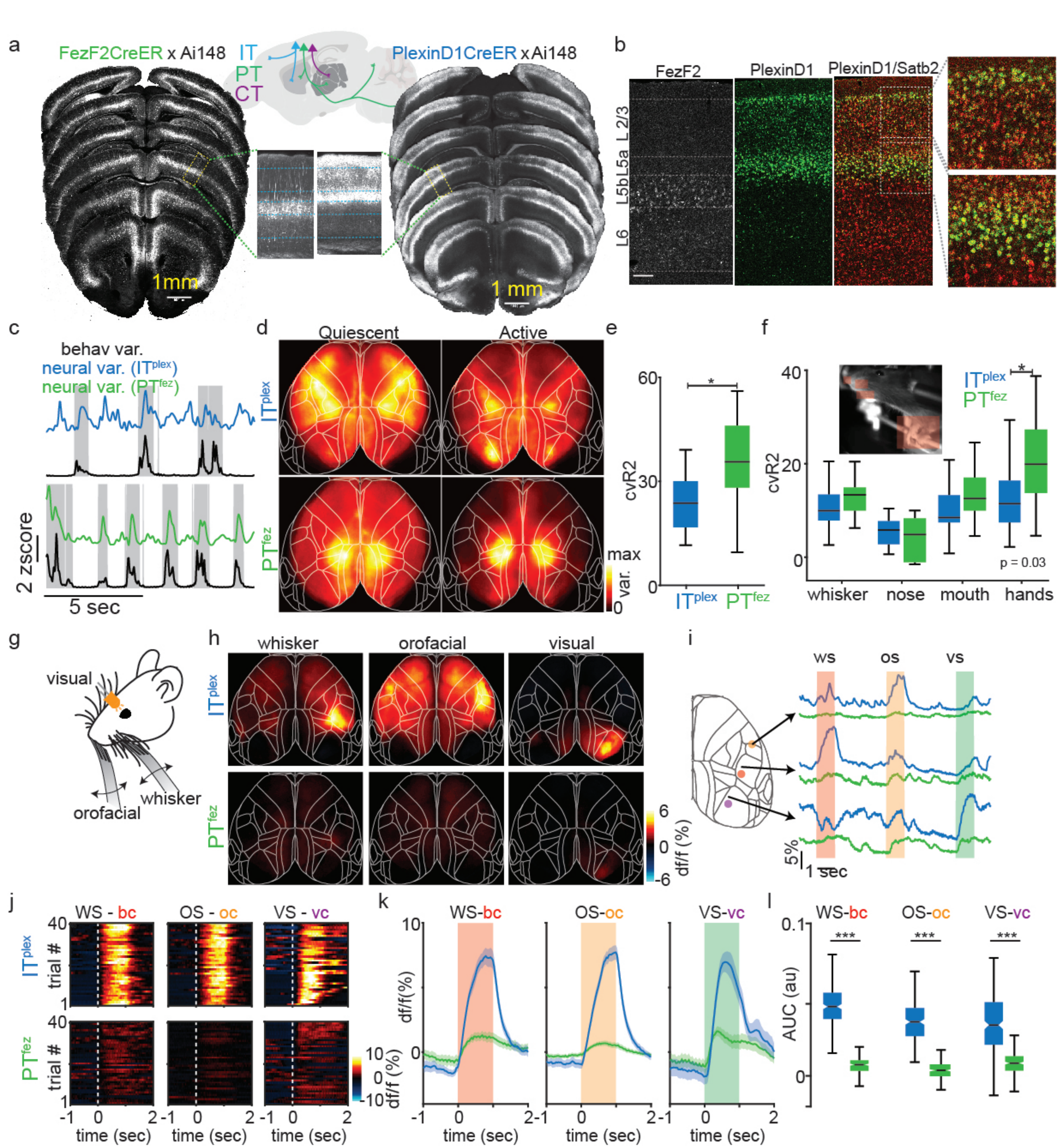
a
FezF2CreER x Ai148
IT
PT
CT
PlexinD1CreER x Ai148
1mm
1 mm
b
FezF2
PlexinD1
PlexinD1/Satb2
L 2/3
L5b L5a
L6
c
behav var.
neural var. (ITplex)
neural var. (PTfez)
2 zscore
5 sec
d
Quiescent
Active
ITplex
PTfez
max
var.
0
e
60
30
0
cvR2
*
ITplex
PTfez
f
40
20
0
cvR2
ITplex
PTfez
*
p = 0.03
whisker
nose
mouth
hands
g
visual
whisker
orofacial
h
whisker
orofacial
visual
ITplex
PTfez
6
0
-6
df/f (%)
i
ws
os
vs
5%
1 sec
j
WS - bc
OS - oc
VS - vc
ITplex
PTfez
trial #
40
1
-1
0
2
time (sec)
10
0
-10
k
WS-bc
OS-oc
VS-vc
df/f(%)
df/f (%)
l
WS-bc
OS-oc
VS-vc
0.1
0
AUC (au)
***

figure 1

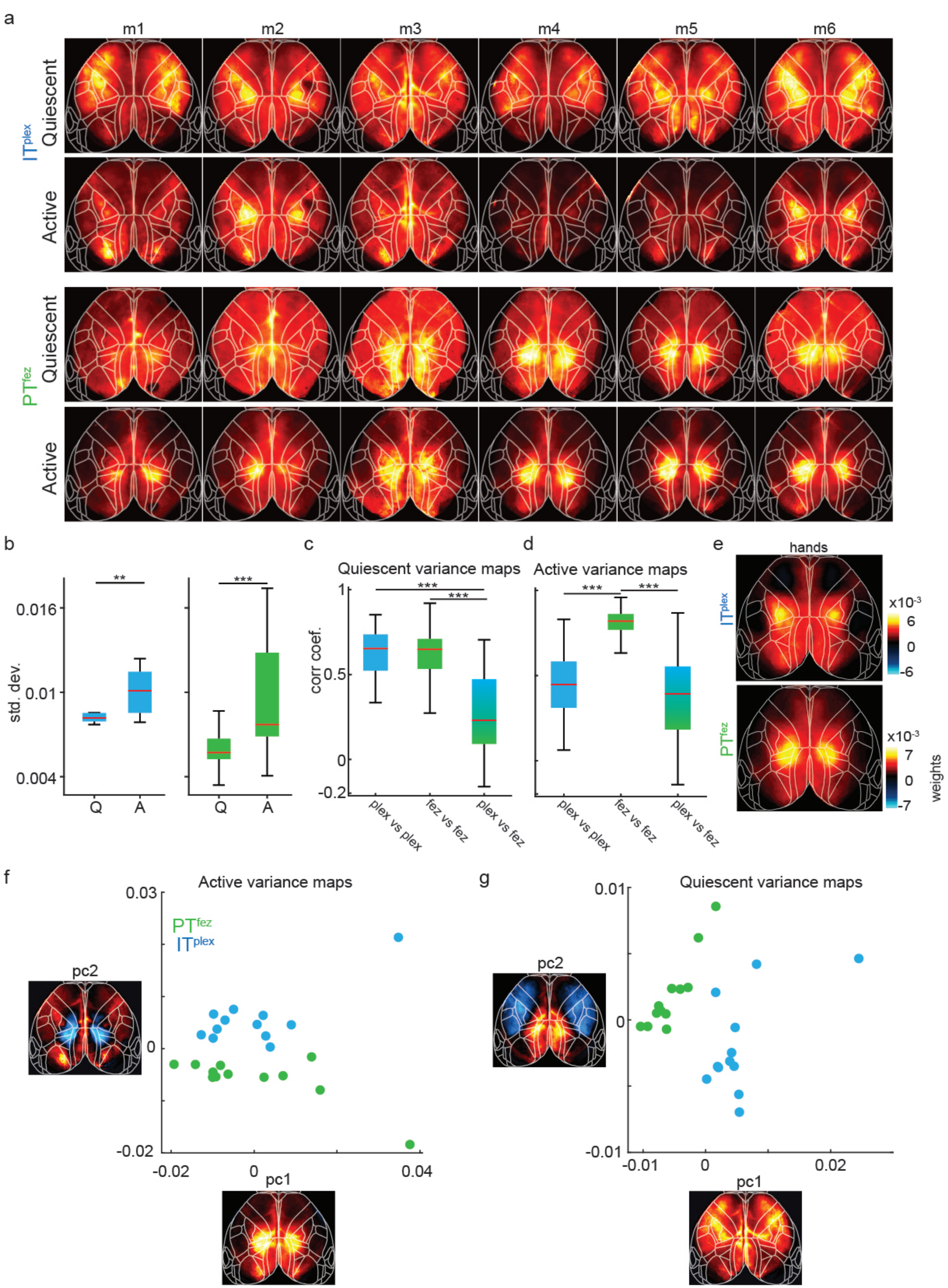

figure 1. suppl. fig. 1

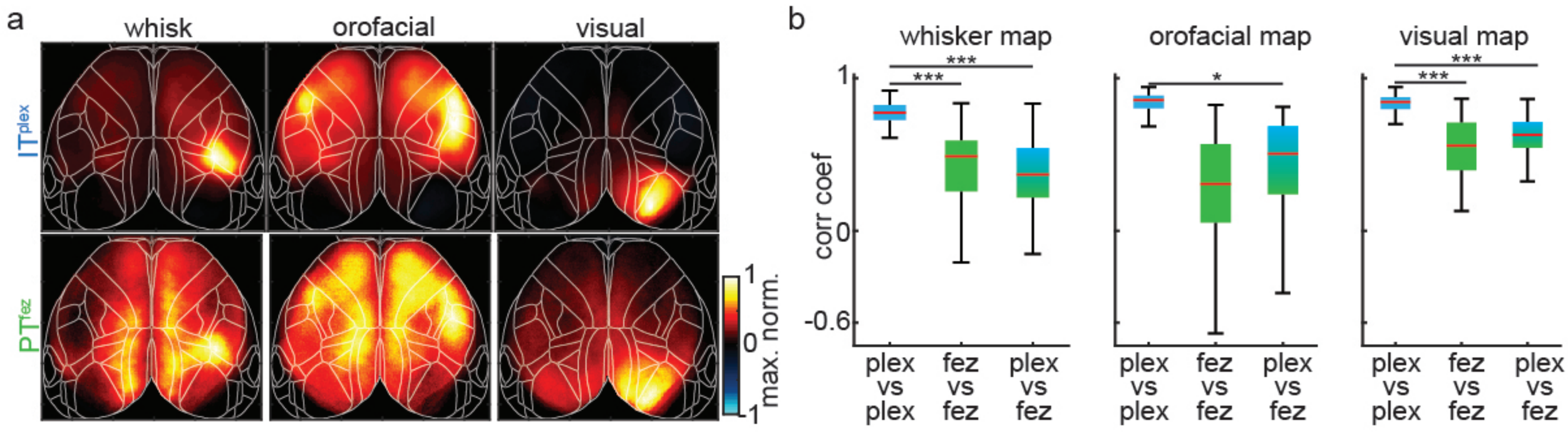

figure 1 suppl. fig. 2

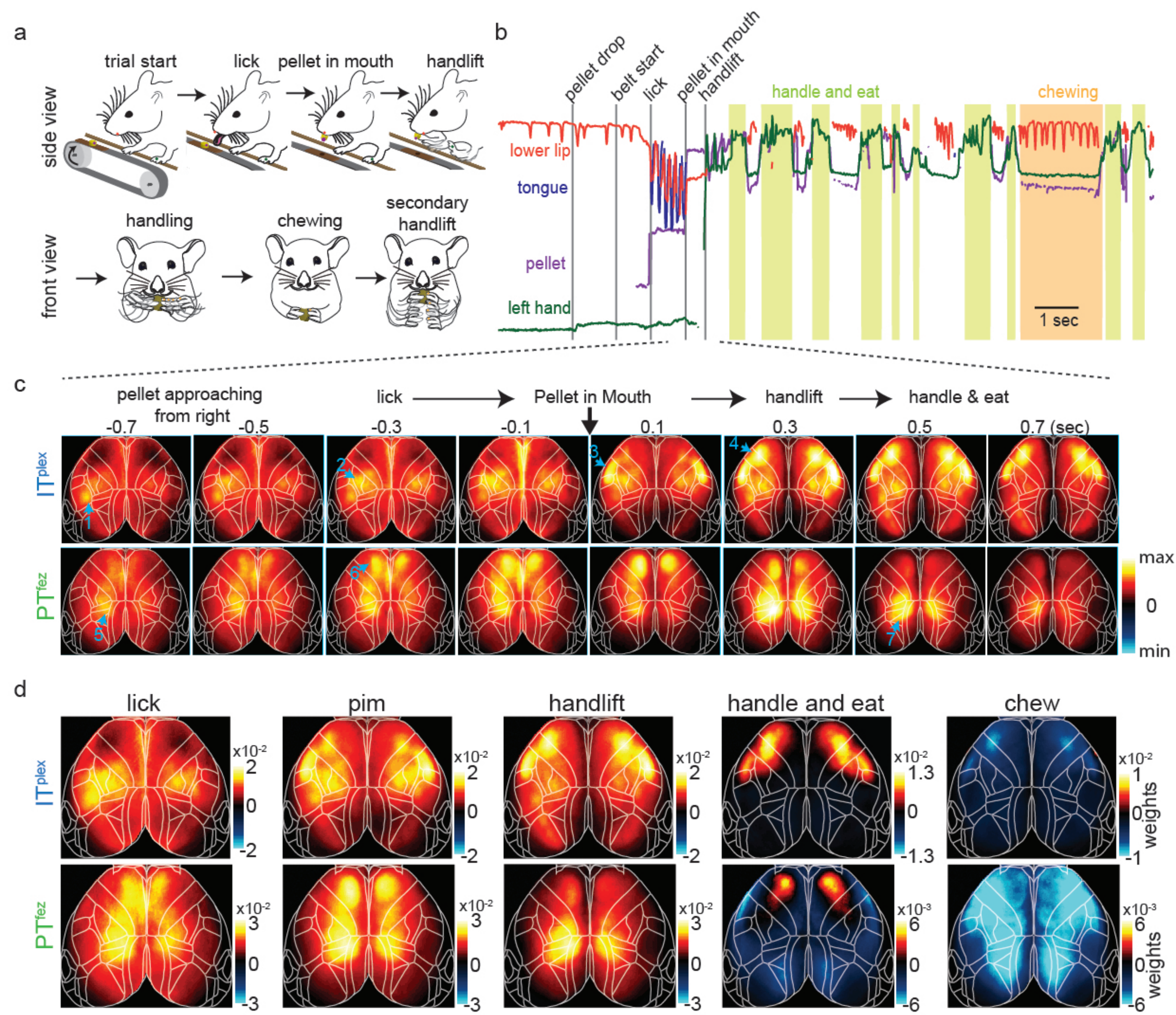
a
trial start
lick
pellet in mouth
handlift
side view
handling
chewing
secondary handlift
front view
b
pellet drop
belt start
lick
pellet in mouth
handlift
handle and eat
chewing
lower lip
tongue
pellet
left hand
1 sec
c
pellet approaching from right
lick
Pellet in Mouth
handlift
handle & eat
-0.7
-0.5
-0.3
-0.1
0.1
0.3
0.5
0.7 (sec)
ITplex
PTfez
max
0
min
d
lick
pim
handlift
handle and eat
chew
ITplex
PTfez
x10-2
x10-3
weights

figure 2

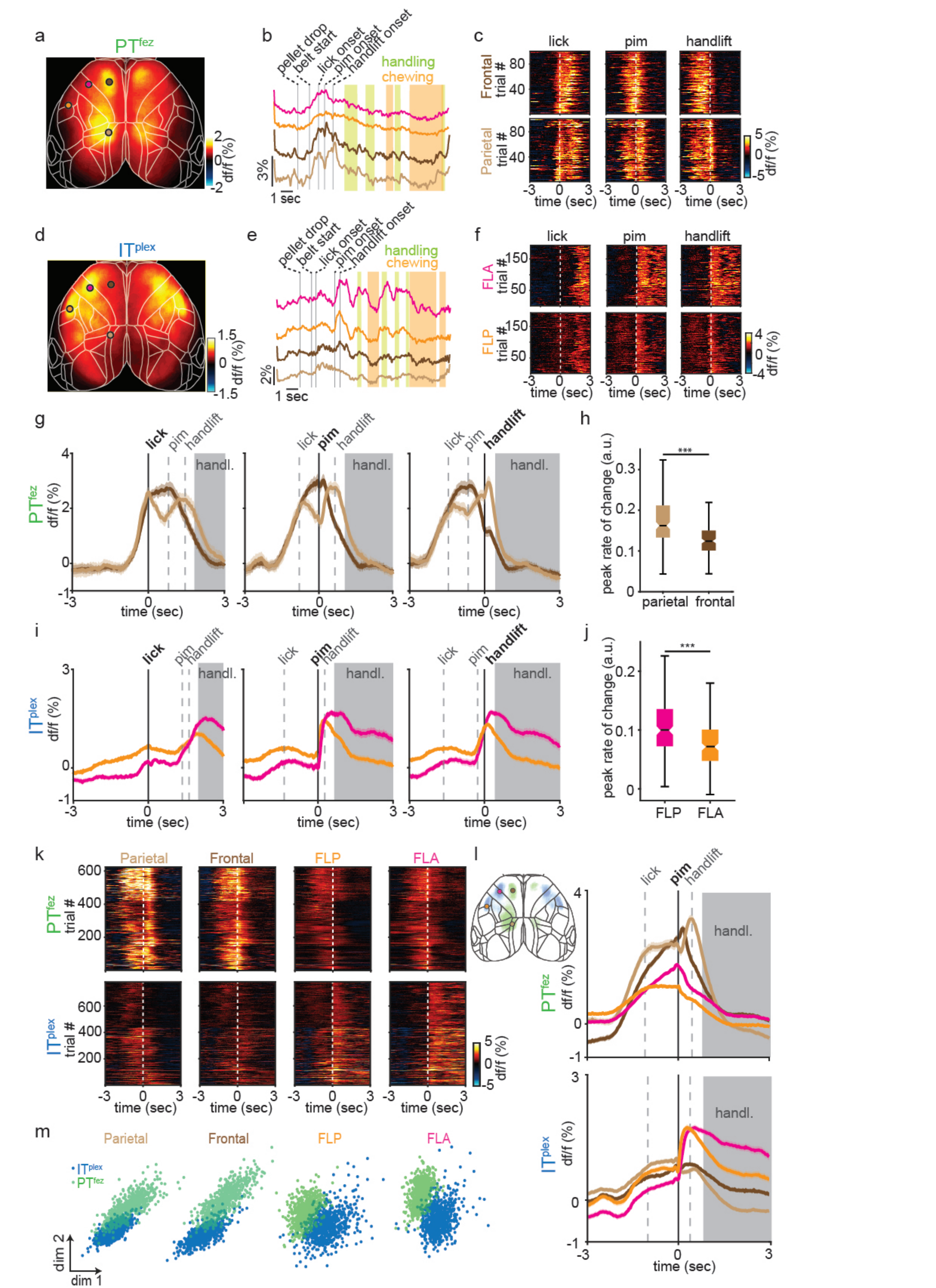
a
PTfez
2
0
-2
df/f (%)
b
pellet drop
belt start
lick onset
pim onset
handlift onset
handling
chewing
3%
1 sec
c
lick
pim
handlift
Frontal
trial #
80
40
Parietal
trial #
80
40
5
0
-5
df/f (%)
-3
0
3
time (sec)
d
ITplex
1.5
0
-1.5
df/f (%)
e
pellet drop
belt start
lick onset
pim onset
handlift onset
handling
chewing
2%
1 sec
f
lick
pim
handlift
FLA
trial #
150
50
FLP
trial #
150
50
4
0
-4
df/f (%)
-3
0
3
time (sec)
g
lick
pim
handlift
handl.
PTfez
df/f (%)
4
2
0
-1
-3
0
3
time (sec)
h
***
peak rate of change (a.u.)
0.3
0.2
0.1
0
parietal
frontal
i
lick
pim
handlift
handl.
ITplex
df/f (%)
3
0
-1
-3
0
3
time (sec)
j
***
peak rate of change (a.u.)
0.2
0.1
0
FLP
FLA
k
Parietal
Frontal
FLP
FLA
PTfez
trial #
600
400
200
ITplex
trial #
600
400
200
5
0
-5
df/f (%)
-3
0
3
time (sec)
l
4
0
-1
PTfez
df/f (%)
lick
pim
handlift
handl.
3
0
-1
ITplex
df/f (%)
handl.
-3
0
3
time (sec)
m
Parietal
Frontal
FLP
FLA
ITplex
PTfez
dim 2
dim 1

figure 3

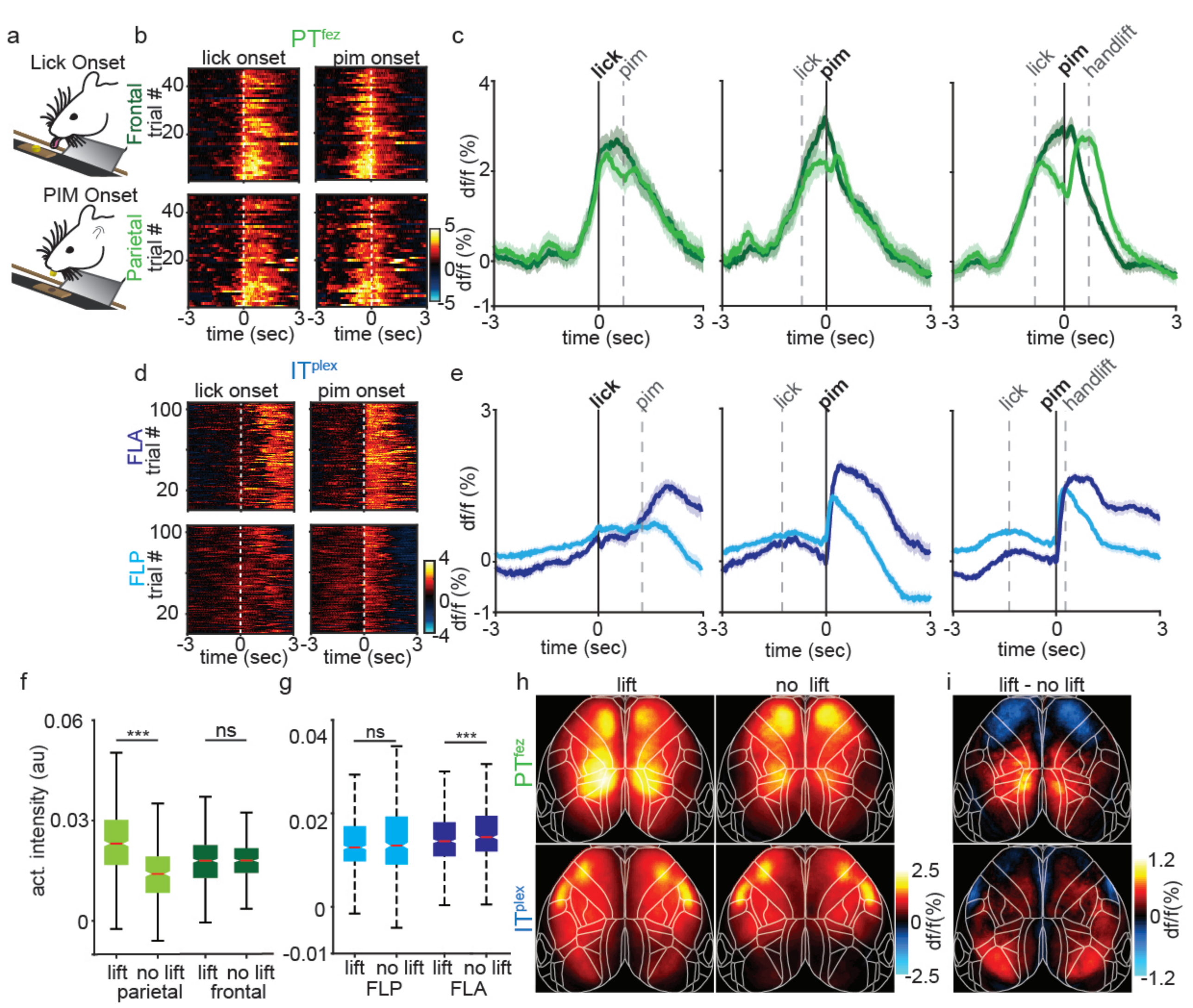
a
Lick Onset
PIM Onset
b
PTfez
lick onset
pim onset
Frontal
Parietal
trial #
time (sec)
c
lick
pim
handlift
df/f (%)
d
ITplex
FLA
FLP
e
f
act. intensity (au)
***
ns
lift
no lift
parietal
frontal
g
FLP
FLA
h
lift
no lift
i
lift - no lift
df/f(%)

figure 4

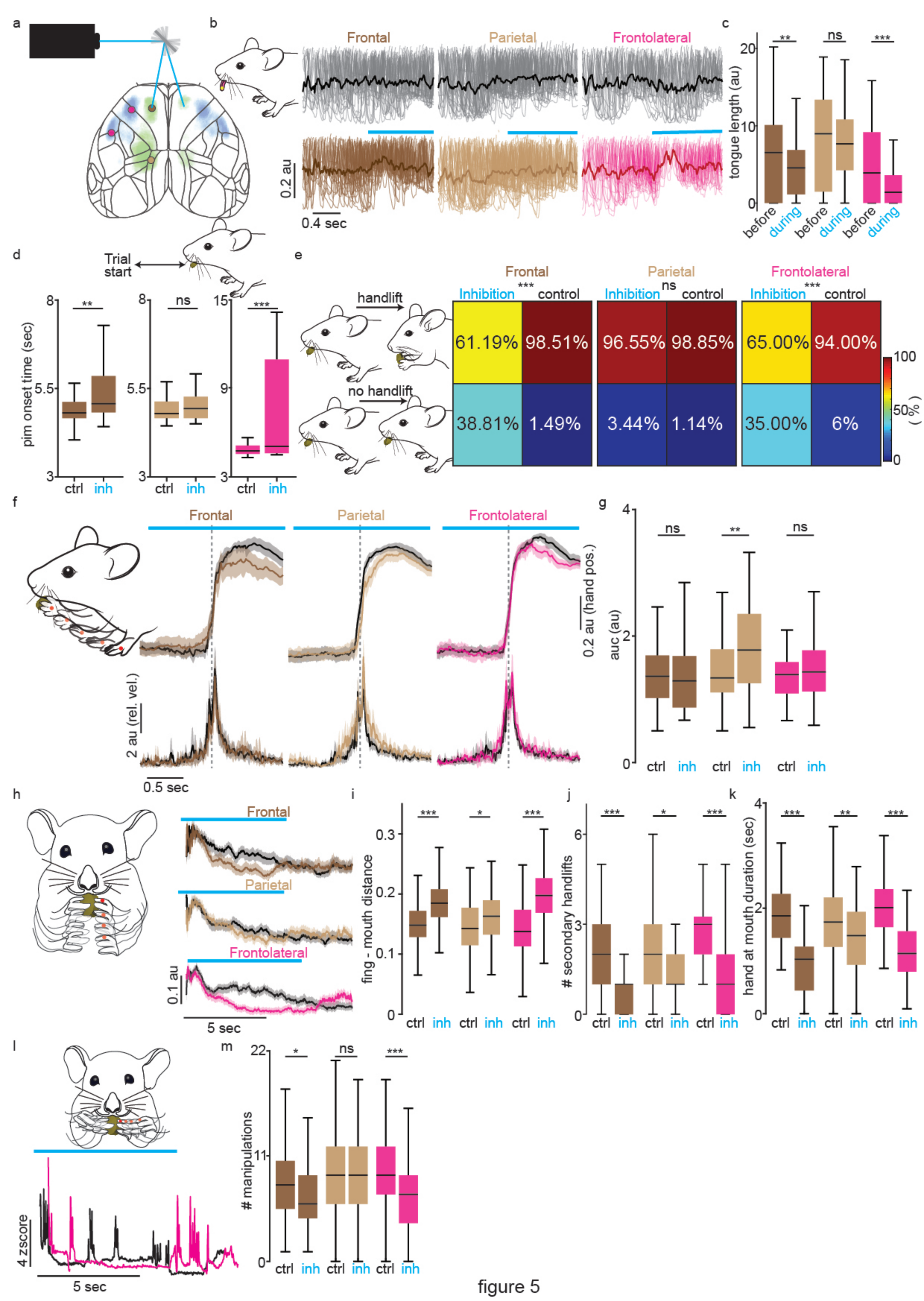
a
b
Frontal
Parietal
Frontolateral
0.2 au
0.4 sec
c
tongue length (au)
before
during
d
Trial start
pim onset time (sec)
ctrl
inh
e
handlift
no handlift
Inhibition
control
61.19%
98.51%
96.55%
98.85%
65.00%
94.00%
38.81%
1.49%
3.44%
1.14%
35.00%
6%
(%)
f
2 au (rel. vel.)
0.5 sec
g
0.2 au (hand pos.)
auc (au)
h
0.1 au
5 sec
i
fing - mouth distance
j
secondary handlifts
k
hand at mouth duration (sec)
l
4 zscore
5 sec
m
manipulations

figure 5

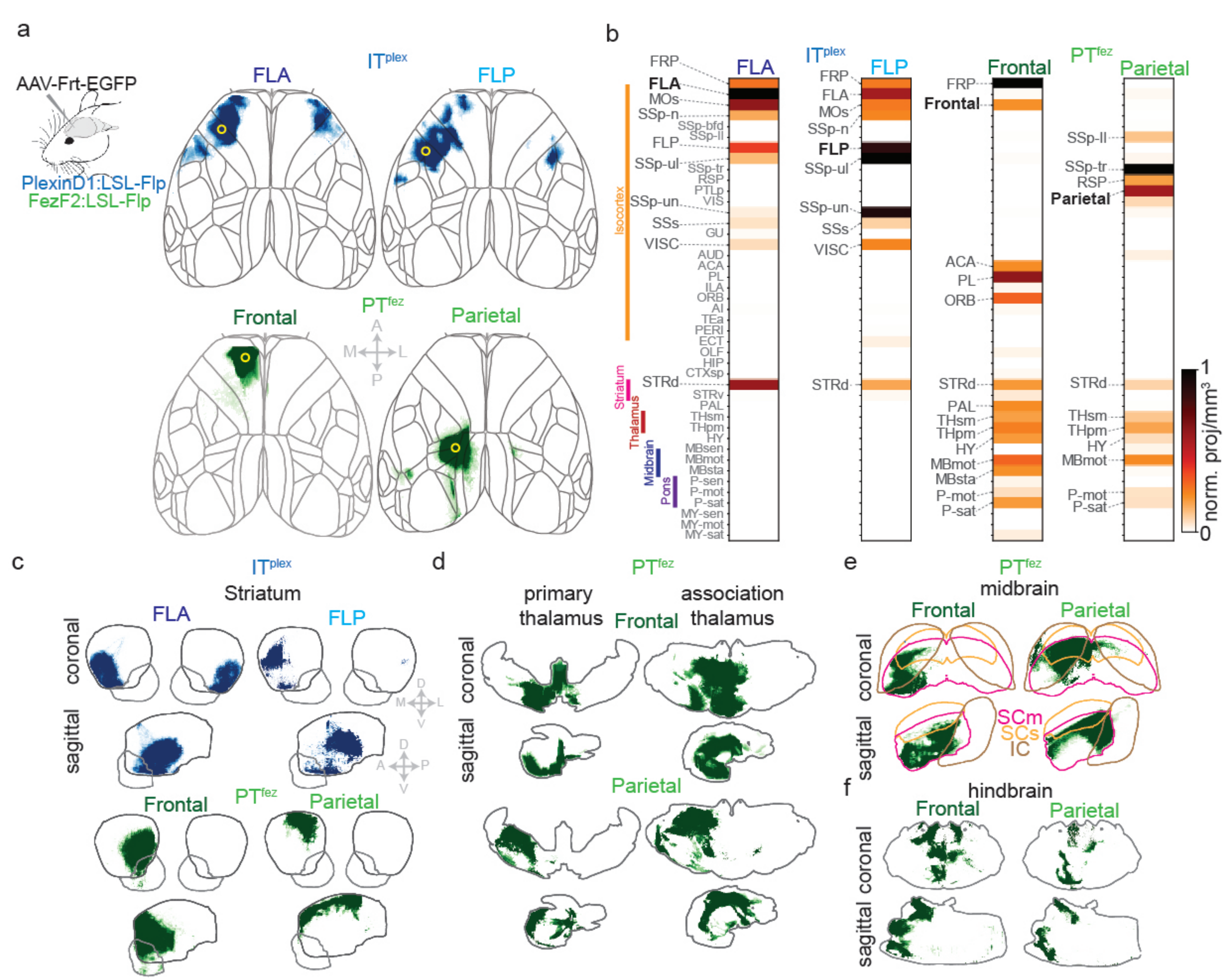
a
AAV-Frt-EGFP
PlexinD1:LSL-Flp
FezF2:LSL-Flp
FLA
ITplex
FLP
Frontal
PTfez
Parietal
A
M
L
P
b
FLA
ITplex
FLP
Frontal
PTfez
Parietal
Isocortex
Striatum
Thalamus
Midbrain
Pons
FRP
FLA
MOs
SSp-n
SSp-bfd
SSp-ll
FLP
SSp-ul
SSp-tr
RSP
PTLp
VIS
SSp-un
SSs
GU
VISC
AUD
ACA
PL
ILA
ORB
AI
TEa
PERI
ECT
OLF
HIP
CTXsp
STRd
STRv
PAL
THsm
THpm
HY
MBsen
MBmot
MBsta
P-sen
P-mot
P-sat
MY-sen
MY-mot
MY-sat
Frontal
ACA
PL
ORB
Parietal
SSp-ll
SSp-tr
RSP
1
0
norm. proj/mm³
c
ITplex
Striatum
FLA
FLP
coronal
sagittal
D
M
L
V
A
P
Frontal
PTfez
Parietal
d
PTfez
primary thalamus
Frontal
association thalamus
coronal
sagittal
Parietal
e
PTfez
midbrain
Frontal
Parietal
coronal
sagittal
SCm
SCs
IC
f
hindbrain
Frontal
Parietal
coronal
sagittal

figure 6

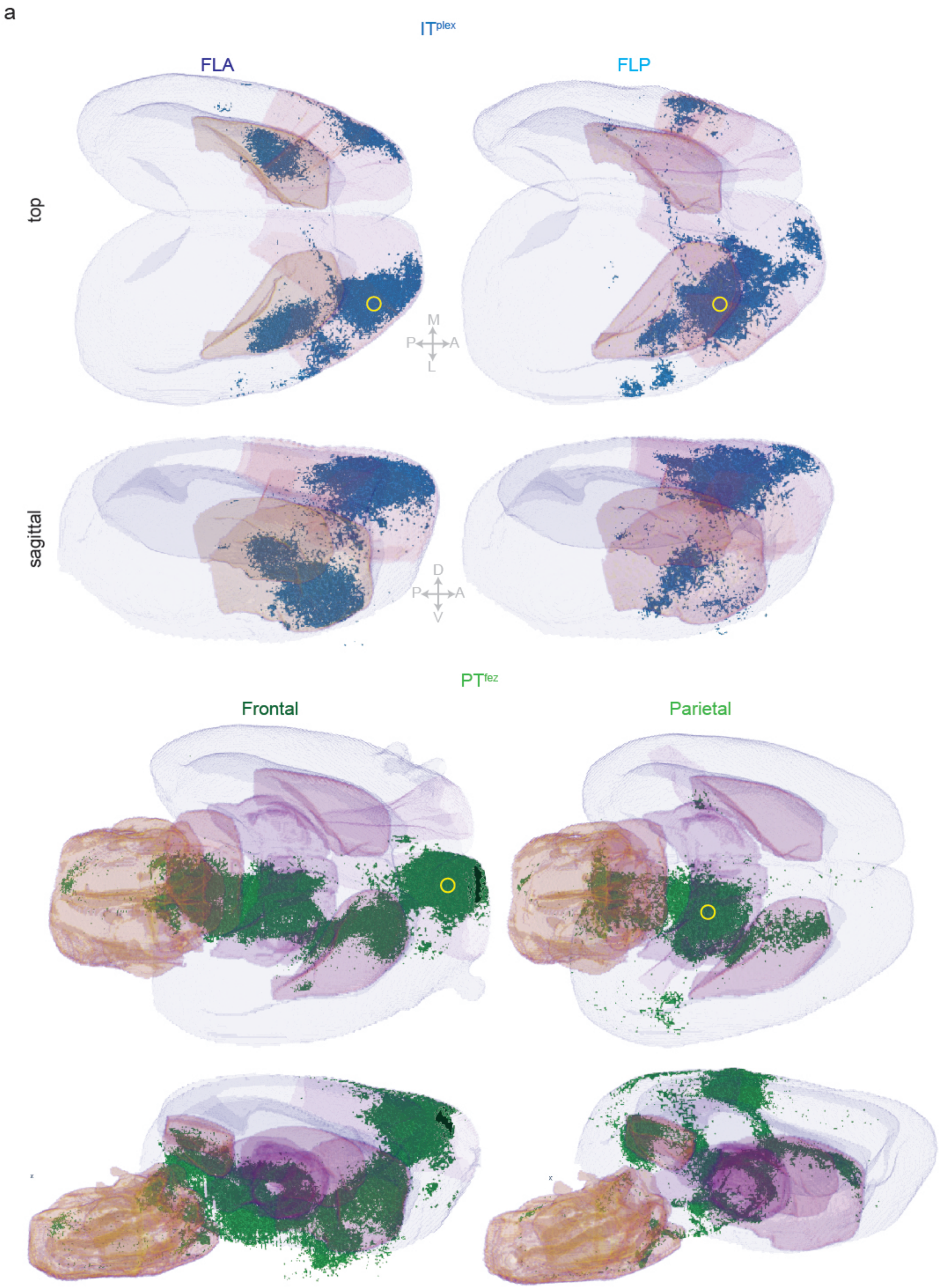

figure 6 Suppl. fig. 3

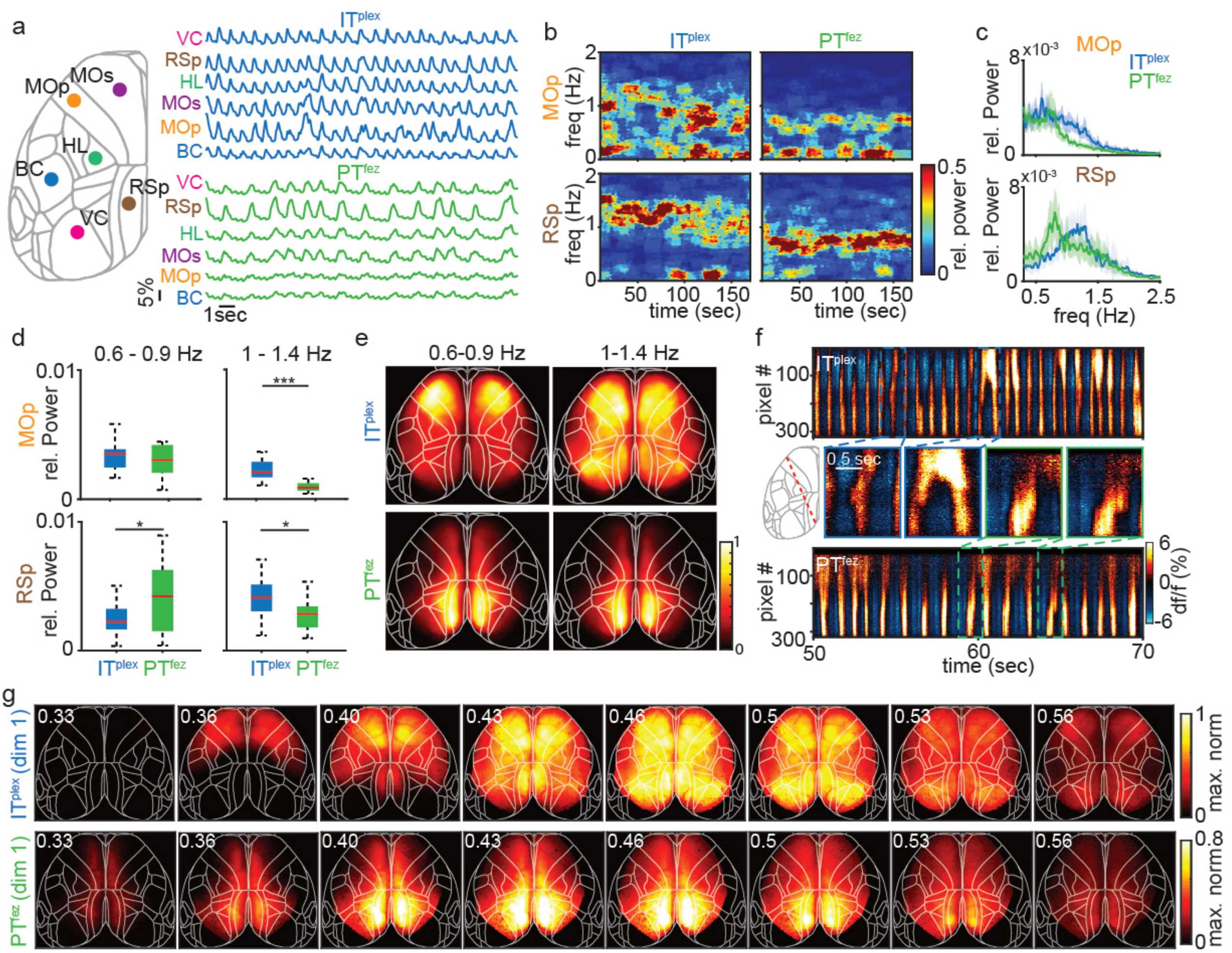
a
MOp
MOs
HL
BC
RSp
VC
ITplex
PTfez
5%
1sec
b
MOp
RSp
freq (Hz)
time (sec)
rel. power
c
MOp
RSp
rel. Power
freq (Hz)
d
0.6 - 0.9 Hz
1 - 1.4 Hz
MOp
RSp
rel. Power
e
0.6-0.9 Hz
1-1.4 Hz
f
pixel #
0.5 sec
df/f (%)
time (sec)
g
(dim 1)
max. norm

figure 7